rate. Using the filtered back-projection for the image reconstruction is another reason of the limited quality of the phantom images. Optimization of the system parameters such as lower energy level or time window may improve the image quality in somehow. Also applying an iterative image reconstruction will improve the image quality of the PET system.

V. Conclusion

We have successfully developed the PET-Hat for brain research. The PET-Hat could be measured in the sitting position of the subject and could move with the subject. We conclude that the PET-Hat is promising, low cost, small size, wearable brain PET system for brain functional studies.

Acknowledgment

The authors would like thank to Mr. Ohta of Eiko-Sangyo Co. for designing and constructing the mechanical part of the PET-Hat system.

References

[1] P. T. Fox, M. A. Mintun, M. E. Raichle, F. M. Miezin, J. M. Allman, and D. C. Van Essen, "Mapping human visual cortex with positron emission tomography," *Nature*, vol. 323, pp. 806–809, Oct. 1986.

[2] S. E. Petersen, P. T. Fox, A. Z. Snyder, and M. E. Raichle, "Activation of extrastriate and frontal cortical areas by visual words and word-like stimuli," *Science*, vol. 249, no. 4972, pp. 1041–1044, 1990.

[3] M. Corbetta, F. M. Miezin, S. Dobmeyer, G. L. Shulman, and S. E. Petersen, "Attentional modulation of neural processing of shape, color and velocity in humans," *Science*, vol. 248, no. 4962, pp. 1556–1559, 1990.

[4] P. T. Fox, M. E. Mintun, M. E. Raichle, and P. P. Herscovitch, "A noninvasive approach to quantitative functional brain mapping with H2 (15)O and positron emission tomography," *J. Cereb. Blood Flow Metab.*, vol. 4, no. 3, pp. 329–333, 1984.

[5] S. Ogawa, T. M. Lee, A. R. Kay, and D. W. Tank, "Brain magnetic resonance imaging with contrast dependent on blood oxygenation," *Proc. Natl. Academy Sciences USA*, vol. 87, no. 24, pp. 9868–9872, 1990.

[6] S. Ogawa, T. M. Lee, and G. Barrere, "The sensitivity of magnetic resonance image signals of a rat brain to changes in the cerebral venous blood oxygenation," *Magn. Reson. Med.*, vol. 29, no. 2, pp. 205–210, 1993.

[7] I. Eshed, C. E. Althoff, B. Hamm, and K. G. Hermann, "Claustrophobia and premature termination of magnetic resonance imaging examinations," *J. Magn. Reson. Imag.*, vol. 26, no. 2, pp. 401–404, 2007.

[8] S. Thorpe, P. M. Salkovskis, and A. A. Dittner, *Magn. Reson. Imag. Claustrophobia in MRI: The Role of Cognitions*, vol. 26, no. 8, pp. 1081–1088, 2008.

[9] M. Teräs, T. Tolvanen, J. J. Johansson, J. J. Williams, and J. Knuuti, "Performance of the new generation of whole-body PET/CT scanners: Discovery STE and discovery VCT," *Eur. J. Nucl. Med. Mol. Imag.*, vol. 34, no. 10, pp. 1683–1692, 2007.

[10] K. Matsumoto *et al.*, "Performance characteristics of a new 3-dimensional continuous-emission and spiral-transmission high-sensitivity and high-resolution PET camera evaluated with the NEMA NU 2-2001 standard," *J. Nucl. Med.*, vol. 47, no. 1, pp. 83–90, 2006.

[11] S. Surti, A. Kuhn, M. E. Werner, A. E. Perkins, J. Kolthammer, and J. S. Karp, "Performance of philips gemini TF PET/CT scanner with special consideration for its time-of-flight imaging capabilities," *J. Nucl. Med.*, vol. 48, no. 3, pp. 471–480, 2007.

[12] G. Brix *et al.*, "Performance evaluation of a whole-body PET scanner using the NEMA protocol. National electrical manufacturers association," *J. Nucl. Med.*, vol. 38, no. 10, pp. 1614–1623, 1997.

[13] T. Oohasi *et al.*, "In audible high-frequency sound affect brain activity: Hypersonic effect," *J. Neuriphysiol.*, vol. 83, no. 6, pp. 2548–2558, 2000.

[14] J. S. Karp, S. Surti, M. E. Daube-Witherspoon, R. Freifelder, C. A. Cardi, L. E. Adam, K. Bilger, and G. Muehllehner, "Performance of a brain PET camera based on anger-logic gadolinium oxyorthosilicate detectors," *J. Nucl. Med.*, vol. 44, no. 8, pp. 1340–1349, 2003.

[15] H. W. de Jong, F. H. van Velden, R. W. Kloet, F. L. Buijs, R. Boellaard, and A. A. Lammertsma, "Performance evaluation of the ECAT HRRT: An LSO-LYSO double layer high resolution, high sensitivity scanner," *Phys. Med. Biol.*, vol. 52, no. 5, pp. 1505–1526, 2007.

[16] E. Yoshida *et al.*, "Design and inital evaluation of a 4-layer DOI-PET system: The jPET-D4," *Igaku Butsuri.*, vol. 26, no. 3, pp. 131–140, 2006.

[17] D. L. Bailey, T. Jones, T. J. Spinks, M. C. Gilardi, and D. W. Townsend, "Noise equivalent count measurements in a neuro-PET scanner with retractable septa," *IEEE Trans. Med. Imag.*, vol. 10, no. 3, pp. 256–260, 1991.

[18] M. Watanabe *et al.*, "A new high-resolution PET scanner dedicated to brain research," *IEEE Trans. Nucl. Sci.*, vol. 49, no. 3, pp. 634–639, Jun. 2002.

[19] S. Yamamoto and H. Ishibashi, "A GSO depth of interaction detector for PET," *IEEE Trans. Nucl. Sci.*, vol. 45, no. 3, pp. 1078–1082, Jun. 1998.

[20] S. Yamamoto, "A dual layer DOI GSO block detector for a small animal PET," *Nucl. Instrum. Methods Phys. Res. A*, vol. A598, pp. 480–484, 2008.

[21] R. Pani, M. N. Cinti, R. Pellegrini, C. Trotta, G. Trotta, L. Montani, S. Ridolfi, F. Garibaldi, R. Scafè, N. Belcari, and A. D. Guerra, "Evaluation of flat panel PMT for gamma ray imaging," *Nucl. Instrum. Methods Phys. Res. A*, vol. A504, pp. 262–268, 2003.

[22] S. Yamamoto, H. Mashino, H. Kudo, K. Matsumoto, and M. Senda, "A dual layer GSO PET system for small animal: K-PET II," *IFMBE Proc.*, vol. 14, pp. 1712–1715, 2007.

[23] S. Yamamoto, "Optimization of the integration time of pulse shape analysis for dual layer detector with different amount of Ce," *Nucl. Instrum. Methods Phys. Res. A*, vol. A587, pp. 319–323, 2008.

[24] M. E. Daube-Witherspoon *et al.*, "PET performance measurements using the NEMA NU 2-2001 standard," *Nucl. Med.*, vol. 43, no. 10, pp. 1398–1409, 2002.

[25] E. J. Hoffman, P. D. Cutler, W. M. Digby, and C. J. Mazziotta, "3-D phantom to simulate cerebral blood flow and metabolic images for PET," *IEEE Trans. Nucl. Sci.*, vol. 37, no. 2, pp. 616–620, Apr., 1990.

NeuroImage 56 (2011) 1469–1479

Contents lists available at ScienceDirect

NeuroImage

journal homepage: www.elsevier.com/locate/ynimg

Time course and spatial distribution of fMRI signal changes during single-pulse transcranial magnetic stimulation to the primary motor cortex

H. Shitara [a,b], T. Shinozaki [b], K. Takagishi [b], M. Honda [a], T. Hanakawa [a,c,*]

[a] Department of Functional Brain Research, National Institute of Neuroscience, National Center of Neurology and Psychiatry, Japan
[b] Department of Orthopedic Surgery, Gunma University Graduate School of Medicine, Japan
[c] PRESTO, Japan Science and Technology Agency, Japan

ARTICLE INFO

Article history:
Received 19 November 2010
Revised 27 February 2011
Accepted 3 March 2011
Available online 9 March 2011

Keywords:
Motor cortex
Muscle afferent
Blood oxygenation-dependent signals
Functional magnetic resonance imaging

ABSTRACT

Simultaneous transcranial magnetic stimulation (TMS) and functional magnetic resonance imaging (fMRI) may advance the understanding of neurophysiological mechanisms of TMS. However, it remains unclear if TMS induces fMRI signal changes consistent with the standard hemodynamic response function (HRF) in both local and remote regions. To address this issue, we delivered single-pulse TMS to the left M1 during simultaneous recoding of electromyography and time-resolved fMRI in 36 healthy participants. First, we examined the time-course of fMRI signals during supra- and subthreshold single-pulse TMS in comparison with those during voluntary right hand movement and electrical stimulation to the right median nerve (MNS). All conditions yielded comparable time-courses of fMRI signals, showing that HRF would generally provide reasonable estimates for TMS-evoked activity in the motor areas. However, a clear undershoot following the signal peak was observed only during subthreshold TMS in the left M1, suggesting a small but meaningful difference between the locally and remotely TMS-evoked activities. Second, we compared the spatial distribution of activity across the conditions. Suprathreshold TMS-evoked activity overlapped not only with voluntary movement-related activity but also partially with MNS-induced activity, yielding overlapped areas of activity around the stimulated M1. The present study has provided the first experimental evidence that motor area activity during suprathreshold TMS likely includes activity for processing of muscle afferents. A method should be developed to control the effects of muscle afferents for fair interpretation of TMS-induced motor area activity during suprathreshold TMS to M1.

Introduction

Transcranial magnetic stimulation (TMS) is now widely applied to basic and clinical studies in neuroscience. However, the mechanisms of how TMS influences behavior are not completely clear. It is conceivable that TMS most strongly influences neural activity beneath the TMS coil, but it has been proven that TMS can also modulate neural activity in the remote regions (Paus et al., 1997). Advance in technology now allows for combining TMS and functional magnetic resonance imaging (fMRI), which can measure locally and remotely induced activity changes in the whole brain (Bestmann et al., 2003; Bohning et al., 1998; Hanakawa et al., 2009).

Previous TMS-fMRI studies have measured TMS-induced changes of blood-oxygenation level-dependent (BOLD) signals, which are widely used as a surrogate marker of the summation of synaptic/neuronal activity. The BOLD contrast reflects hemodynamic changes involving a complex interaction between levels of oxygenation, blood flow and blood volume (Nair, 2005; Wang et al., 2004). The coupling mechanisms of synaptic/neuronal activity and BOLD signals remain ambiguous although BOLD signals show reasonable correlation with synaptic and neuronal activities measured with electrophysiological methods (Logothetis, 2000; Ogawa et al., 2000). Notably, recent studies have shown that TMS may change cerebrovascular reactivity (Rollnik et al., 2002; Sallustio et al., 2010). Since the sympathetic nervous system regulates reactivity of the cerebral vasculature, possible interference of TMS with sympathetic regulation may explain this finding. Alternatively, TMS could disrupt functions of the local circuitry consisting of interneurons and astrocytes, regulating dilation of arterioles (Zonta et al., 2003). Since TMS would most strongly influence the region beneath the coil, we cannot exclude the possibility that TMS may particularly affect the neurovascular coupling of the stimulated site. Previously, near-infrared spectroscopy (NIRS) was applied to examine the time-course of hemodynamic signal changes following single-pulse TMS. One study reported increases in oxyhemoglobin after both single-pulse TMS and voluntary movement (Noguchi et al., 2003) while another one found marked decreases in deoxyhemoglobin without increases in oxyhemoglobin and total hemoglobin (Mochizuki

* Corresponding author at: Department of Functional Brain Research, National Institute of Neuroscience, National Center of Neurology and Psychiatry, 4-1-1 Ogawahigashi, Kodaira 187-8502, Japan.
E-mail address: hanakawa@ncnp.go.jp (T. Hanakawa).

1053-8119/$ – see front matter © 2011 Elsevier Inc. All rights reserved.
doi:10.1016/j.neuroimage.2011.03.011

et al., 2006). This discrepancy may partly stem from the possible disruption of hemodynamic responses during TMS.

Previous TMS-fMRI studies applying TMS to the primary motor cortex (M1) consistently reported activity in local and remote motor areas during TMS. Intriguingly, the directly stimulated M1 shows significantly increased activity only with stimulation above the level of resting motor threshold (RMT) whereas the remote motor areas including the supplementary motor areas (SMA) showed significant activity below the RMT (Bestmann et al., 2003; Fox et al., 2006; Hanakawa et al., 2009; Speer et al., 2003). It remains unknown why remote motor areas show blood flow changes at lower stimulation intensities than does the M1 on which TMS should exert a direct impact. This paradox could at least in part result from the fact that the previous TMS-fMRI studies employed standard hemodynamic response functions (HRF) to detect BOLD signal changes. That is, the profile of BOLD signal changes in M1 beneath the TMS coil could differ from that in remote motor areas because of the possible disruption of normal neurovascular coupling.

In the present study, we conducted an fMRI experiment to characterize the time-course and spatial distribution of BOLD signal changes evoked by TMS in the motor areas. Previous research has described the time-course of TMS-evoked activities using a block-design fMRI (Bestmann et al., 2004; Bohning et al., 1999), which precludes a fine analysis of the signal time-course in response to each stimulus. The primary purpose of the present study was thus to examine time-course of fMRI signal changes following single-pulse TMS with a finer temporal resolution than ever. This knowledge should provide an important basis to justify the comparison of the spatial distribution of fMRI activity during TMS with that during other tasks shown to induce HRF-compatible fMRI signal changes. After gaining knowledge on the time-course of TMS-induced activity, we then compared the spatial distribution of activity during single-pulse TMS with that during motor and somatosensory reference conditions. The reference conditions included cued voluntary movement and electrical median nerve stimulation (MNS), both of which involved the same effector with the TMS. The findings suggested the effects of muscle afferents onto motor area activity during suprathreshold TMS to the M1.

Experimental procedures

Subjects

Thirty-six healthy adults (mean age = 27.0 years; range 20–46 years) participated in the present experiment. None of the participants reported any history of neuropsychiatric disorders, including epilepsy. All participants were right handed. The review board of the National Center of Neurology and Psychiatry approved the study protocol. The subjects were fully informed about the experimental procedure, and all gave written informed consent prior to participation.

Stimulation and electromyography monitoring

A 3-Tesla whole-body MRI scanner equipped with a circular polarization head coil (Siemens Magnetom Trio; Erlangen, Germany) was used for the experiment. We delivered TMS to the hand representation of the left M1 (M1-hand). The "motor hot spot" where TMS evoked a maximal motor response in the right abductor pollicis brevis (APB) muscle was identified for each participant while lying supine on the scanner bed. The APB was the primary muscle of interest in this experiment, in accord with our previous experiment (Hanakawa et al., 2009). An MRI-compatible figure-of-eight TMS coil with an outer-wing diameter of 70 mm (MR coil, Magstim, Witland, Wales, UK) was positioned tangentially to the scalp at the "motor hot-spot". The orientation of the TMS coil was approximately 45° from the medial–lateral axis. The TMS coil was connected to a stimulator (SuperRapid, Magstim, Witland, Wales, UK) via a 7-m cable running through a wave guide tube appropriate for radiofrequency wave filtering. The TMS stimulator produced biphasic electrical pulses of approximately 250-μs duration and a rise time of 50 μs.

For the MNS-fMRI experiment, electrical stimulation was delivered through a pair of MRI-compatible electrodes (Nihon Kohden, Tokyo, Japan). The electrodes were connected to an electric current stimulator (Nihon Kohden, Tokyo, Japan) placed outside the scanner room. The maximum stimulator output was 50 mV. Constant-voltage square waves with a pulse duration of 0.3 ms were applied to the right median nerve at the wrist. The sensory threshold was determined by each participant's verbal report of sensation in the first three fingers without muscle twitching. A motor threshold for eliciting APB activity was determined with EMG monitoring in each participant. No participants reported a sensation of pain. The electrical stimulation procedure did not cause any artifacts in the functional MR images.

EMG was monitored and recorded during the fMRI experiments. For EMG recording during fMRI, we used a modified version of the "stepping-stone sampling" (SSS) method (Hanakawa et al., 2009), which was originally developed for combined electroencephalography and fMRI recording (Anami et al., 2003). In 14 participants who underwent the TMS-fMRI experiment only, motor evoked potentials (MEPs) were recorded from the right APB and the right abductor digiti minimi (ADM) muscles using SynAmps (Neuroscan, Sterling, VA, USA). Surface electrodes with shielded plates and cables were placed over the right APB and ADM muscles with an inter-electrode distance of approximately 2 cm. In the rest of the subjects, MEPs were recorded from the bilateral APB and ADM muscles using BrainAmp ExG MR (Brain Products, Gilching, Germany). EMG signals were fed to a digital amplifier electrically through a radiofrequency filter (SynAmps) or to a battery-driven amplifier placed on the scanner bed (BrainAmp ExG MR). A ground electrode was placed on the dorsal surface of the right wrist. As the SSS method requires exact synchronization between the timing of EMG sampling and that of gradient pulses for MRI acquisition, the SynAmps amplifier was externally driven by the clock of the MRI scanner. For this purpose, the clock frequency was down-sampled from the original 10 MHz to 10 kHz using a custom-made clock divider (CD5; Physio-Tech, Tokyo, Japan). Furthermore, trigger pulses from the scanner were sent to the CD 5 clock divider to synchronize the onset of EMG measurement and MRI acquisition. For EMG recorded with BrainAmp ExG MR, the amplifier and MRI scanner were synchronized using SyncBox (Brain Products, Gilching, Germany) to receive the clock and trigger signals from the scanner. EMG data were either sampled at a digitization rate of 1 kHz with an amplitude resolution of 0.336 μV/bit and a dynamic range of 22 mV (SynAmps), or a digitization rate of 5 kHz with an amplitude resolution of 0.5 μV/bit and a dynamic range of 16 mV (BrainAmp ExG MR). The data sampled with BrainAmp ExG MR were down-sampled from 5 kHz to 1 kHz to match the sampling rate of the data from SynAmp at a later processing stage.

Isometric contraction was employed for all types of movements in the present experiment. Custom-made, non-magnetic splints covering the hand, wrist and elbow joints were used to restrict the movement of the upper limbs on both sides. Then, both upper limbs were tightly fixed with elastic bandages and taped onto the splints. The setup was intended to minimize joint movements, and the effects of antagonistic muscles due to stretching. In addition, the fixation of the hand position should minimize changes of EMG and the shape of imaging artifacts on EMG over time. The position of the TMS coil was adjusted while stimulation was delivered every 5 s to elicit stable production of MEPs from the right APB muscle. The TMS coil was then fixed immobile to the scanner bed with a custom-made holder made from polyetheretherketone plastic. Foam pads and vacuum cushions were used to minimize head motion during scanning. After the participant's head was positioned at the MRI gantry center, the RMT was defined individually

as the percentage of stimulator output that elicited MEPs of >50 μV peak-to-peak amplitude in the APB in the state of rest in more than five of 10 successive trials (Rossini et al., 1994). The active motor threshold (AMT) was similarly determined during weak and sustained contraction of the APB muscle under EMG monitoring.

Experimental tasks

During the fMRI experiments, participants were instructed to relax and to remain awake. Vision was not constrained. In each fMRI run, 42 single-pulse TMS or MNS stimuli were given during inter-volume acquisition delay periods with a semi-randomized stimulus onset asynchrony (SOA) between 7.98 and 13.97 s (stimulus frequency = 0.072–0.125 Hz). Fifteen participants underwent the TMS&MNS-fMRI experiment, 17 participants underwent the TMS-fMRI experiment only, and four participants underwent the MNS-fMRI experiment only. In the TMS-fMRI experiment, participants underwent three fMRI runs (one for each experimental condition). The experimental conditions were composed of suprathreshold TMS with an intensity of 120% of the RMT ('supra-TMS'), subthreshold TMS with an intensity of 90% of the AMT ('sub-TMS'), and a motor reference task. In the TMS&MNS-fMRI experiment, all participants underwent a single fMRI run for the supra-TMS, motor reference task, MNS above the motor threshold ('motor-MNS'), and MNS between the sensory and the motor thresholds ('sensory-MNS'). The sensory-MNS condition was included to account for stimulation of sensory components of the median nerve stimulation. Eight participants underwent an additional fMRI run for the motor-MNS condition. Stimulus intensity for the motor-MNS was semi-randomly varied between the motor threshold and 120% of the motor threshold to yield similar variability in evoked movement size as in the supra-TMS condition. The intensity of sensory-MNS was kept constant below the motor threshold and above the sensory threshold in all participants.

As a motor reference task, participants performed a single fMRI run for cued voluntary movement (VM) in response to a click sound produced by the TMS with intensity of 30% of the machine output. We have previously shown that stimulation at this intensity with MRI-compatible TMS does not change motor network activity (Hanakawa et al., 2009). As such, stimulation should have only served as an auditory cue. Brain activity information from the VM task was used to setup volumes of interest (VOIs), and to serve as a reference for the time-course analysis.

The stimulation timing was controlled by Presentation software (Neurobehavioral systems, Albany, CA, USA) on a personal computer synchronized with the MRI scanner via transistor–transistor logic pulses converted from the default optic signals of the scanner. To avoid image degradation, TMS pulses were delivered during 110-ms inter-volume delay periods, during which no gradient magnetic fields or radiofrequency pulses were generated for MRI acquisition. The same stimulation timing was used for the motor- or sensory-MNS conditions. The order of the conditions was semi-randomized across the subjects.

Image acquisition

The SSS method was used to measure hemodynamic signals with a blip-type echo planar imaging (EPI) sequence with the following parameters: repetition time (TR) = 998 ms, inter-volume acquisition delay = 110 ms, echo time (TE) = 25 ms, flip angle (FA) = 60°, 64 × 64 matrix, 12 slices, 500 volumes, field of view (FOV) = 192 mm, 3 × 3 × 4-mm voxel size, and bandwidth = 1086 Hz. In the SSS-EPI sequence, the timing of gradient pulses was carefully designed so that electrophysiological signals could be sampled at 1 kHz while avoiding the effects of gradient pulses (Anami et al., 2003; Hanakawa et al., 2009). To maintain consistency of the timing of gradient pulses and electrophysiological sampling, the scanner and EMG amplifier were synchronized as described above. The functional images covered the bilateral cortical motor and somatosensory areas, basal ganglia and thalami, with approximately coronal acquisition. Most of the cerebellum was outside of the search volume. We employed a relatively short TR and limited the search volume. This experimental setup was chosen to investigate the signal time-course of TMS-evoked activity in the motor cortices and the basal ganglia with fine temporal resolution. The inter-volume acquisition delay allowed us to acquire SSS-EPI data without interference from induced electromagnetic fields or vibration of the TMS coil.

For anatomic registration, T1-weighted three-dimensional structural images were also acquired with a magnetization-prepared, rapid-gradient echo sequence (TR = 2,000 ms, TE = 4.38 ms, FA = 8°, FOV = 192 mm, matrix = 176 × 192, voxel size = 1 × 1 × 1 mm). For distortion correction of functional images, field map images were obtained in the same space as the functional image (TR = 511 ms, TE = 5.19 and 7.65 ms, FA = 60°, FOV = 192 mm, matrix = 64 × 64, voxel size = 3 × 3 × 4 mm).

EMG and image data analysis

To remove gradient artifacts, all EMG data were processed using the averaged subtraction method implemented with Analyzer 2 software (Brain Products, Gilching, Germany). A band-pass filter of 20–200 Hz was applied. Artifact-removed EMG data from the left APB and bilateral ADM muscles were checked to confirm the absence of muscle activity in non-target muscles.

The imaging data were pre-processed with SPM5 (Wellcome Department of Imaging Neuroscience, UCL, London, UK) implemented on Matlab7 (MathWorks, Inc., Natick, MA, USA) and FSL (FMRIB, Oxford University, Oxford, UK) implemented on VMware player (VMware, Palo Alto, CA, USA). The first 10 volumes in each experimental run were discarded to allow for T1 equilibrium effects. The remaining functional images were corrected for differences in slice acquisition timing. The distortion of EPI data resulting from inhomogeneity of the magnetic field was corrected using FUGUE (FSL), by referencing to the field map acquired for each participant before the fMRI experiment. The functional images were motion-corrected, and residual noises were detected and removed with an independent component analysis filter (MELODIC, FSL). The motion-corrected and artifact-removed images were then spatially normalized to fit the Montreal Neurological Institute (MNI) template based on the standard stereotaxic coordinate system. Subsequently, all images were smoothed with an isotropic Gaussian kernel of 8-mm full-width at half-maximum (FWHM).

A statistical analysis was performed using SPM5. A vector representing the event onsets were modeled as a main regressor for the first-level general linear model (GLM) analysis. This analysis was performed for each participant to test the correlation between fMRI signal changes and a train of delta functions (representing the stimulus onsets) convolved with the canonical HRF and its temporal derivative. Six parameters representing the head motion were included in the design matrix as covariates of no interest. Global signal normalization was performed only between runs. Low frequency noise was removed with a 128-s high-pass filter, and serial correlations were adjusted using an auto-regression model. We computed summary images reflecting the effects of interest on fMRI signals by applying linear contrasts to the parameter estimates. These summary images were fed into the subsequent second-level random-effect model analysis.

Time-course analysis of fMRI signal changes

It was not clear if BOLD signal changes after TMS followed the standard HRF. This uncertainty is especially problematic when single-pulse TMS is used in an event-related fMRI design. Although we assumed the standard HRF following single-pulse TMS in a previous

study (Hanakawa et al., 2009), we might actually have underestimated activity in the M1 if BOLD signal changes in the directly stimulated site fitted poorly to the standard HRF.

In the present study, by capitalizing on relatively fine sampling of fMRI signals and long interstimulus intervals, the time-course of fMRI signal changes following the TMS events was referenced to those after the VM and motor-MNS events. The fMRI signal time-course was extracted from representative VOIs determined on an *a priori* basis using the results from the VM condition as a reference. The representative areas included the bilateral M1, the left dorsal premotor area (PMd), the supplementary motor area (SMA), the left primary somatosensory area (S1), the left subthalamic nucleus (STN), the left putamen, and the ventrolateral nucleus of the left thalamus. The signal time-series was extracted from spherical VOIs with a 5-mm radius, except for the STN where a 3-mm radius was used because of its small size. These data were converted into percent signal changes, using the signal value at the stimulus event as a baseline. The center of each VOI was determined according to the local maxima of the second-level SPMs for the VM condition. The center coordinates were applied to each participant's data to retrieve time-series information. A relatively ventral part of the SMA adjoining the caudal cingulate zone (CCZ) within the cingulate sulcus was sampled on the basis of our previous findings of SMA activation during M1 stimulation (Hanakawa et al., 2009). This selection of SMA as a VOI was expected to help avoid sampling from the vascular structure in the midline (Bohning et al., 1999). The VOIs for the STN, putamen and thalamus were consistent with the corresponding activities shown in previous fMRI studies (Aron and Poldrack, 2006; Zhang et al., 2008). Initially, the time-course was compared across the conditions using VOI-based signal averaging followed by statistical analyses. For exploring slight differences in signal time-course across the conditions, a more precise analysis was performed by calculating the ratio between the effect size estimated for canonical HRF ($\beta 1$) and that of its temporal derivative. We used information from the data variance captured by the temporal derivative of the canonical HRF to detect subtle differences in the peak latency of fMRI signals. The temporal derivative is a first-order Taylor expansion of the HRF. Positive or negative effects captured by the temporal derivative in the first-level GLM analysis mean that the peaks of fMRI signals in the data were slightly earlier or later than those of the canonical HRF, respectively (Henson et al., 2002). Given that the $\beta 1$ was positive, the positive and negative signs of $\beta 2/\beta 1$ indicate that the peak of fMRI responses was earlier and later, respectively, than that of the canonical HRF.

Spatial pattern analyses assuming HRF

After the time-course of fMRI signal changes during single-pulse TMS was assessed, statistical parametric maps were created for each condition. Group-level statistical parametric maps (SPMs) were generated by performing one-sample t-tests on the summary images representing the effects of each experimental condition relative to baseline from the HRF-based first-level analysis. Conditional differences in evoked brain activity were tested between the supra-TMS and sub-TMS conditions and between the motor-MNS and sensory-MNS conditions. In the group-level SPM, the threshold was initially set at a voxel-wise height-level of $P<0.05$ corrected for multiple comparisons (family-wise error; FWE). Based on the previous simultaneous TMS-neuroimaging studies comparing activity between TMS to M1-hand and hand movement conditions (Siebner et al., 1998; Bestmann et al., 2003), we hypothesized that TMS to left M1-hand would activate the motor network for right hand movement. We also hypothesized that afferent information associated with twitching of left thenar muscles would be fed to the same network. Therefore, we applied a small volume correction (SVC) analysis to the group-level SPMs by using the same set of VOI for the time-course analysis (Table 1). Clusters exceeding a height threshold of uncorrected $P<0.001$ were reported as a trend when it was deemed appropriate. The cytoarchitectonic nomenclature of significant brain activity was identified according to the SPM anatomy toolbox (Eickhoff et al., 2005) when applicable.

Results

TMS intensity

The mean RMT and AMT were 79.6% (SD = 9.0) and 69.3% (10.2) of the machine output, respectively, within the MRI scanner. Accordingly, the mean stimulus intensity for the supra-TMS condition was 95.2% (10.8) and that for the sub-TMS condition was 62.5% (9.0). For stimulus intensity above 100% of the machine output, the maximum machine output of the TMS stimulator was temporarily reset to 110% of the default machine output (enhanced mode). All participants completed the planned experimental conditions, and none experienced significant adverse events.

EMG

The quality of the EMG data after the removal of scanning artifacts was satisfactory (Fig. 1). Based on the EMG assessment in each individual, the data from 12 fMRI runs were excluded from further analysis because of a lack of MEPs during the supra-TMS condition (three runs), large stimulation artifacts during the motor-MNS condition (six runs), or unexpected (possibly voluntary) muscle activity during the sub-TMS (one run) and the sensory-MNS (two runs) conditions. These technical problems were partially ascribed to displacement of the body or the coil/electrode positions after the initial experimental setup. In the remaining data set, muscle activity was only observed in the right APB muscle in the supra-TMS, motor-MNS and VM condition. This finding indicated that TMS- or MNS-evoked muscle activity did not spread to the right ADM.

Time-course of TMS-evoked fMRI signals

Time-course changes of fMRI signals were computed by employing VOIs defined by the group-level statistical parametric map of the VM-induced activity (Table 1). In the averaged time-series data using all trials, the signal peak was observed approximately 5–6 s after the events in all conditions (Fig. 2). Since the location of the VOIs depended upon the VM condition only, it was unlikely that the similar time-course across the conditions resulted from sampling bias. A time-course analysis limited to the trials with long inter-trial intervals (12–14 s) clearly showed that the fMRI responses returned to the baseline approximately 10 s after all of the event types. To evaluate the time-

Table 1
Definition of the volumes of interest for the time-course analysis.

Volumes-of-interest	x	y	z
Left primary motor cortex (M1)	−34	−30	64
Right primary motor cortex (M1)*	34	−30	64
Left dorsal premotor cortex (PMd)	−32	−10	60
Left primary somatosensory cortex (S1)	−32	−32	68
Left SMA/CCZ	−6	−12	48
Left putamen	−30	−10	0
Left subthalamic nucleus (STN)	−12	−18	−4
Left thalamus	−14	−22	4

SMA/CCZ; supplementary motor area/caudal cingulate zone. Coordinates were defined using the results from the group-level statistical parametric mapping analysis of the voluntary movement condition (Table 2A).

* The right M1, in which there was no significant activation in the reference task, was defined by flipping the left M1 coordinates along the y axis.

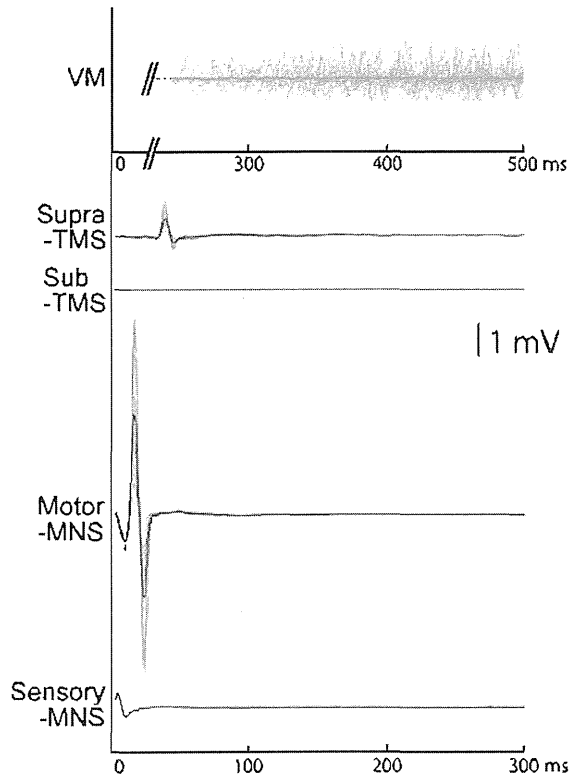

Fig. 1. Electromyography (EMG) during the functional magnetic resonance imaging (fMRI) experiment displayed on a single-trial basis from a representative participant. EMG recording during fMRI was performed using "stepping stone sampling". After post-processing for artifact removal, EMG responses were clearly observed during the voluntary movement, suprathreshold transcranial magnetic stimulation (TMS) and motor-threshold median nerve stimulation (MNS) conditions. No EMG responses were observed during subthreshold TMS or sensory-MNS. It should be noted that polymorphic EMG activity associated with VM lasts much longer than oligophasic EMG associated with suprathreshold TMS and motor-MNS.

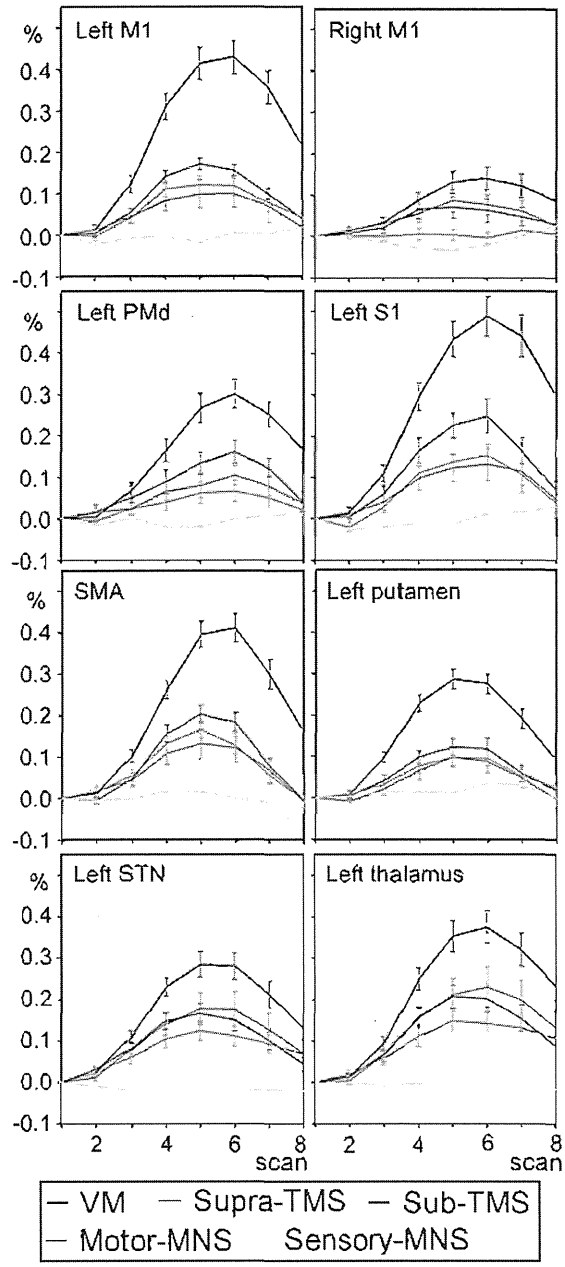

Fig. 2. Time-course of fMRI signal change in the bilateral M1, left PMd, left S1, SMA, left putamen, left STN and left thalamus. The signal value at the time of stimulation (scan 0) was employed as the baseline. The signal value at the time of stimulation (scan 0) was employed as the baseline: the data were converted into percent signal changes and averaged across participants. The error bar represents the standard error of the mean. Blue line = voluntary movement, red line = suprathreshold-TMS, grey line = subthreshold-TMS, green line = motor-median nerve stimulation (motor-MNS).

course of fMRI signals regardless of their sizes, the signal values were proportionally normalized by setting the largest signal value to one in each fMRI run in each participant. The peak-adjusted signal time-course data were then averaged across the participants (Fig. 3). Overall, no significant difference in signal time-course was found across the conditions (i.e., no time-by-task interactions in two-way repeated-measures ANOVA). Notably, however, undershoot (negative responses after returning to the baseline) was evident only in the sub-TMS condition in the M1. This sub-TMS-specific signal undershoot was statistically significant in the left M1, but not in the other areas, when tested in the 11th scan ($P<0.05$, one-way ANOVA followed by Bonferroni's correction for multiple comparisons).

The $\beta 2/\beta 1$ ratio failed to show statistically significant differences across the task conditions (Fig. 4). This finding suggests it is reasonable to apply the canonical HRF to capture signal changes during all TMS, MNS and VM. It may be interesting to perform this analysis across the regions in the supra- or sub-TMS conditions, since slight differences in signal timing could provide information about whether the evoked activity is at the first, second, tertiary or higher orders. In other words, the differences in signal peak timing could possibly indicate that activity was induced via single or multiple synaptic transmissions. However, the pattern in $\beta 2/\beta 1$ ratio was almost identical across the VM, TMS and MNS conditions, which should be associated with different mechanisms for inducing neural activity changes. This meant that the present method did not have a sufficient temporal resolution to resolve this issue.

Spatial distribution of brain activity assuming HRF

Voluntary movement (VM) triggered by TMS click

The VM condition induced significant activity in the classical motor–somatosensory network: the left M1 and S1, bilateral dorsal lateral premotor areas (PMd), SMA extending into caudal and rostral cingulate zones (CCZ and RCZ), parietal operculum (S2), insula, basal ganglia (caudate, putamen, pallidum, and STN), and thalamus (Fig. 5 and Table 2A). Additionally, auditory and cognitive/affective regions (such

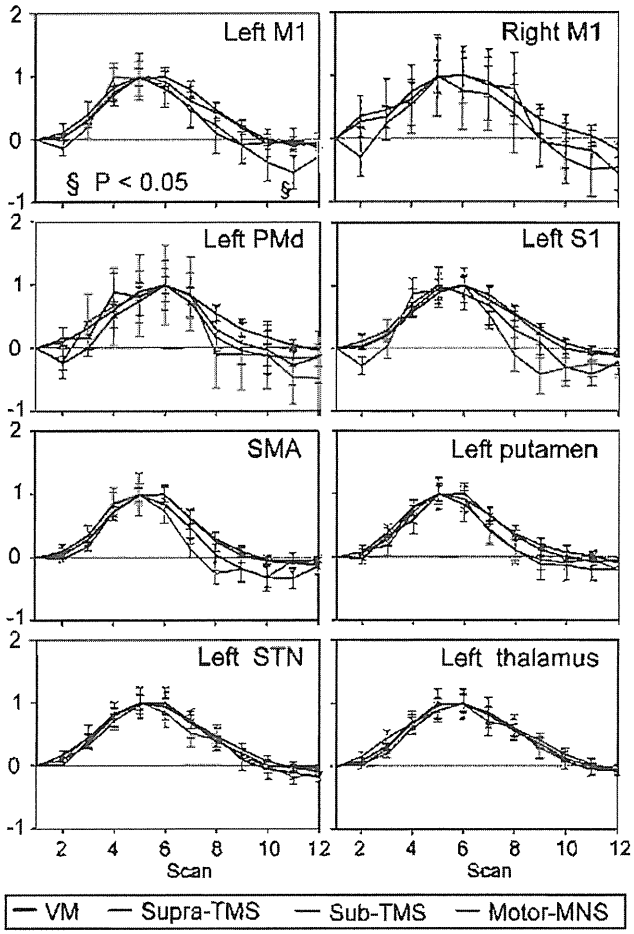

Fig. 3. Signal time-course for 0–12 scans (0–11.98 s) after stimulation. The signal value at the time of stimulation (scan 0) was employed as the baseline. The value of the signal peak in each fMRI run was arbitrarily normalized to one in each fMRI run in each participant; the peak-normalized signal time-course data were averaged across participants. The y-axis represents arbitrary units. The error bar represents the standard error of the mean. Blue line = voluntary movement, red line = suprathreshold-TMS, grey line = subthreshold-TMS, green line = motor-median nerve stimulation (motor-MNS). Undershoot in the left M1 was significant for the sub-TMS condition compared with the other conditions at the 11th scan (§ <0.05 by one-way ANOVA followed by Bonferroni's posterior test). This undershoot phenomenon specific to the sub-TMS was not observed in the remote areas. The motor-MNS induced negative signals in the right M1 (plot not shown).

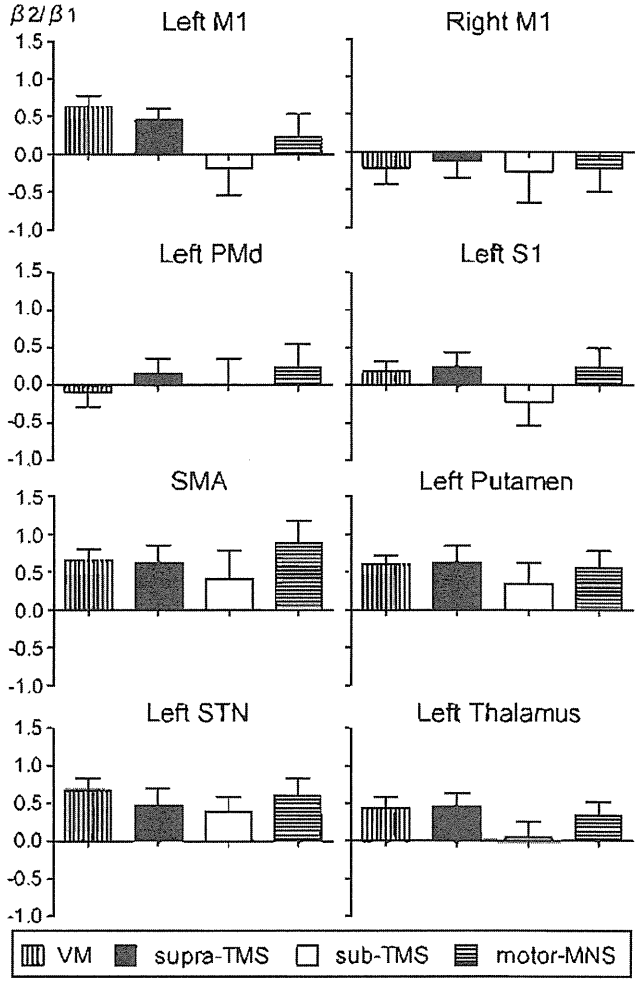

Fig. 4. An analysis of signal time-course was performed by calculating the ratio between the effect size estimated for the canonical HRF (β1) and that of its temporal derivative (β2). Error bars represent SEM.

as the bilateral auditory cortices and hippocampi) were significantly activated.

Supra-TMS

The pattern of activity during the suprathreshold TMS to the M1 (Table 2B) was similar to that during the VM condition as reported previously (Bestmann et al., 2003; Siebner et al., 1998). The left-lateralized activity of the M1 centering on the 'hand-knob' of the precentral gyrus (Yousry et al., 1997) was consistent with activation of the motor representation of the right hand. The activation was more widespread in the bilateral temporal areas including the S2 and auditory areas during the supra-TMS than during the VM condition. This finding was ascribed to the more pronounced click sounds produced in the supra-TMS than in the VM condition.

Sub-TMS

Several areas showed significant activation at the FWE-corrected threshold (bilateral insula, left rolandic operculum, left supramarginal gyrus, bilateral superior temporal gyri, RCZ/CCZ, and left thalamus). Consistent with previous studies (Bestmann et al., 2003; Fox et al., 2006), significant activity ($P<0.05$ FWE-corrected) was found in the left PMd, the left S1, the left SMA, the left putamen, and the left STN in the SVC analysis (Table 2C). However, the SVC analysis failed to find significant activity in the directly stimulated left M1 and the right M1. Additional activity was found in auditory and cognitive/affective regions, including the bilateral auditory cortices, hippocampi, amygdala and middle temporal cortex.

Motor-MNS

The right MNS above the motor threshold induced significant activity relative to the baseline in the left M1, left S1, bilateral PMd, SMA–CCZ/RCZ, bilateral parieto-temporal regions, bilateral insula, left thalamus and bilateral inferior frontal gyri (Table 2D).

Sensory-MNS

There was no significant activation in the sensory-MNS condition relative to baseline at a threshold of $P<0.05$ corrected (FWE). A trend toward activation was found in the RCZ, bilateral insula, bilateral parieto-temporal regions (including S2), and right inferior frontal gyrus ($P<0.001$ uncorrected).

Supra-TMS versus sub-TMS

There were no significant differences in activation between the supra-TMS and sub-TMS conditions at the formal threshold ($P<0.05$,

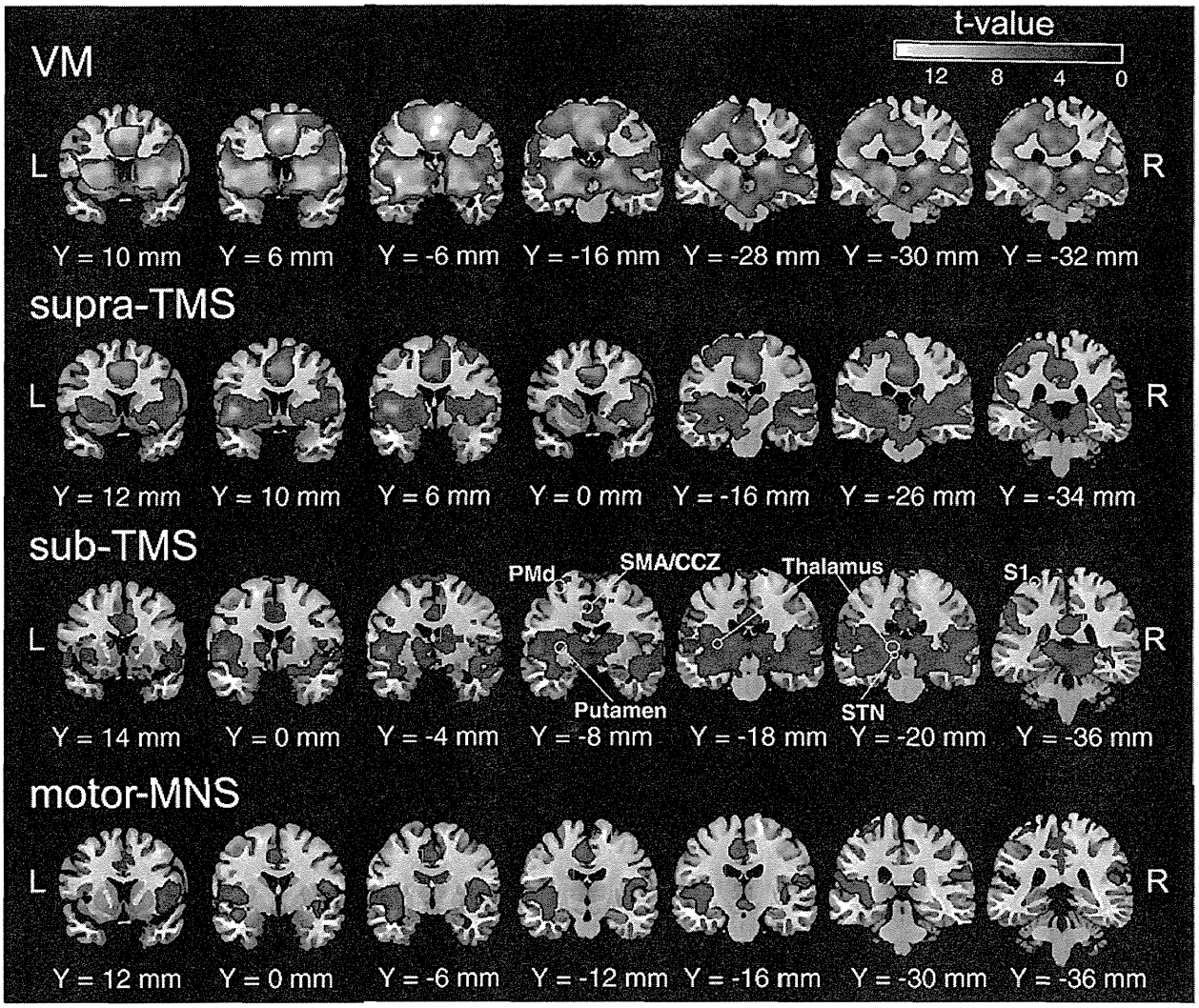

Fig. 5. Group-level statistical parametric maps for the voluntary movement (VM), suprathreshold transcranial magnetic stimulation (supra-TMS) and median nerve stimulation above the motor threshold (motor-TMS) condition. The threshold is set at $P<0.05$ FWE-corrected for multiple comparison in the whole brain. Activity in the sub-TMS condition did not reach significance at the whole-brain threshold. Hence, the threshold for the sub-TMS is set at uncorrected $P<0.001$ for display purpose; the yellow circles indicated the volumes-of-interest used for the small volume correction analysis.

FWE corrected). In the SVC analysis, however, significant activation for the supra-TMS over the sub-TMS was found in the left M1, the left PMd, the left S1, the left SMA/CCZ and the left putamen ($P<0.05$ FWE-corrected). A trend toward increased activation was also found in the left superior temporal gyrus including S2 ($P<0.001$ uncorrected). There was no trend toward activation in the opposite direction (sub-TMS > supra-TMS).

Motor-MNS versus sensory-MNS

This contrast was expected to show neural activity induced by muscle afferents from the thenar muscles since motion of the joints was experimentally constrained by the splints. Only the left S1 showed significant activity at the threshold of $P<0.05$ FWE-corrected for the whole-brain voxels. With the SVC method ($P<0.05$, FWE-corrected), activation was also significant in the left M1, left SMA/CCZ, left putamen, left STN and left thalamus (Fig. 5, Tables 3A and 3B). A trend toward activation was found in the bilateral superior temporal gyri, right thalami, bilateral hippocampi, and bilateral insula (uncorrected $P<0.001$). There was no significant activity or trend in the opposite contrast (sensory-MNS > motor-MNS).

Overlap of supra-TMS minus sub-TMS and motor-MNS minus sensory-MNS

The motor area activity during the motor-MNS compared with the sensory-MNS was located very closely to the region activated during the supra-TMS compared with the sub-TMS (Fig. 6). Application of the SVC method to the intersection of the two activities did reveal the overlap of significant activity in the left M1 (x, y, $z=-36, -30, 66$; $T=3.44$ for the supra-TMS minus sub-TMS and $T=3.87$ for the motor-MNS minus sensory-MNS). The SVC analysis also identified two significant loci in the left S1: (1) x, y, $z=-42, -30, 64$, $T=3.45$ for the supra-TMS minus sub-TMS and $T=4.10$ for motor-MNS minus sensory-MNS and (2) x, y, $z=-32, -32, 66$, $T=3.55$ for the supra-TMS minus sub-TMS and $T=3.78$ for motor-MNS minus sensory-MNS.

Discussion

To our knowledge, the results of the present study provided the first demonstration of the time-course of event-related fMRI signals following single-pulse TMS. Previously, it thus remained ambiguous whether the standard HRF was adequate for detecting TMS-induced activity in both stimulated and remote areas since TMS could

Table 2A
Results from the group-level statistical parametric mapping analysis. Activity associated with voluntary movement (VM).

Activity clusters (functional anatomy)	Coordinates			T-value
	x	y	z	
Right supplementary motor area (SMA)	4	−2	58	16.52
Left middle cingulate region (CCZ)	−2	−6	46	15.74
Left insula	−36	−4	0	15.60
Right supramarginal gyrus (S2)	66	−26	30	14.42
Left rolandic operculum (S2)	−52	2	8	14.35
Right supramarginal gyrus	62	−32	28	13.95
Right putamen	34	4	0	13.90
Right middle cingulate region (CCZ)	8	−20	38	13.35
Right inferior frontal gyrus (Area 44/45)	52	8	8	13.17
Right pallidum	20	0	−6	12.94
Right insula	38	−4	−8	12.69
Left supplementary motor area (SMA)	−6	−12	48	12.35
Left superior temporal gyrus (S2)	−52	−34	16	12.33
Right thalamus	14	−16	14	12.23
Left amygdale	−24	−2	−10	11.99
Left superior temporal gyrus (S2)	−64	−30	20	11.79
Right pallidum	20	−6	8	11.69
Right hippocampus	20	−32	10	11.62
Left precentral gyrus (M1)	−34	−30	64	11.45
Left thalamus	−10	−28	6	11.34
Left precentral gyrus (SMA)	−16	−14	60	10.88
Left putamen	−30	−10	0	10.74
Left postcentral gyrus (S1)	−32	−32	68	9.39
Left thalamus	−14	−22	4	9.05
Left subthalamic nucleus (STN)	−12	−18	−4	8.51
Left precentral gyrus (PMd)	−32	−10	60	7.54

M1 = primary motor cortex, PMd = dorsal premotor cortex, SMA = supplementary motor area, S1 = primary somatosensory cortex, S2 = second somatosensory cortex, RCZ = rostral cingulate zone, S2 = second somatosensory cortex, CCZ = caudal cingulate zone.

Table 2B
Results from the group-level statistical parametric mapping analysis. Activity associated with suprathreshold transcranial magnetic stimulation (120% RMT) applied to the left primary motor cortex.

Activity clusters (functional anatomy)	Coordinates			T-value
	x	y	z	
Left middle cingulate cortex (CCZ)	−4	−8	46	11.67
Left insula	−42	4	4	11.18
Left middle cingulate cortex (RCZ)	−8	10	44	9.75
Right superior temporal gyrus	62	−32	22	9.69
Right superior frontal gyrus	56	12	6	9.61
Left SMA	0	8	48	9.49
Right rolandic operculum (S2)	54	2	10	8.96
Left postcentral gyrus (S1)	−18	−32	70	8.83
Left insula lobe (S2)	−42	−14	8	8.63
Right insula lobe	48	12	−6	8.45
Left superior temporal gyrus (S2)	−62	−26	8	8.45
Right middle temporal gyrus	50	−14	−14	8.25
Left middle temporal gyrus	−42	−26	−8	8.01
Left thalamus	−18	−24	10	7.91
Left pallidum	−10	0	−4	7.78
Left subthalamic nucleus	−6	−18	−6	7.74
Left M1	−30	−30	66	7.51
Left paracentral lobule (SMA/M1)	−6	−22	62	7.40
Right inferior frontal gyrus (Area 44)	44	12	20	7.36
Right thalamus	12	−28	6	7.33
Left precentral gyrus (PMd)	−24	−16	66	7.30
Right Heschl's gyrus (auditory)	36	−26	10	7.26
Left caudate nucleus	−14	12	0	7.25
Right parahippocampal gyrus (hippocampus)	18	−34	−8	7.12
Left putamen	−32	−8	2	7.08
Left STN	−12	−18	−4	6.11
Right M1	24	−30	64	3.91*

M1 = primary motor cortex, PMd = dorsal premotor cortex, SMA = supplementary motor area, S1 = primary somatosensory cortex, S2 = second somatosensory cortex, RCZ = rostral cingulate zone, S2 = second somatosensory cortex, CCZ = caudal cingulate zone.
* Significant with a small volume correction analysis.

Table 2C
Results from the group-level statistical parametric mapping analysis. Activity associated with subthreshold TMS (90% AMT) applied to the left M1.

Activity clusters (functional anatomy)	Coordinates			T-value
	x	y	z	
Left rolandic operculum (S2)	−50	−4	4	10.06
Left supramarginal gyrus (S2)	−58	−28	24	8.37
Left superior temporal gyrus (S2)	−58	−32	14	7.37
Right middle cingulate cortex (RCZ)	8	14	32	7.47
Right insula	42	−2	−8	7.19
Left temporal pole	−56	10	−6	6.84
Left insula	−38	0	10	6.70
Left posterior cingulate cortex (CCZ)	−4	−38	26	6.65
Left thalamus	−16	−18	10	6.62
Right superior temporal gyrus (S2)	56	−18	8	6.61
Left STN	−14	−22	−6	5.00*
Left SMA/CCZ	−2	−8	40	4.48*
Left S1	−32	−36	70	4.23*
Left PMd	−28	−10	68	3.97*
Left putamen	−34	−8	2	3.91*

M1 = primary motor cortex, PMd = dorsal premotor cortex, SMA = supplementary motor area, S1 = primary somatosensory cortex, S2 = second somatosensory cortex, RCZ = rostral cingulate zone, S2 = second somatosensory cortex, CCZ = caudal cingulate zone.
* Significant with a small volume correction analysis.

potentially interfere with vascular reactivity (Rollnik et al., 2002; Sallustio et al., 2010). The setup of VOIs for computing the time-course depended on the VM-induced activity obtained from a GLM analysis assuming the standard HRF. Thus, the time-course of the VM-induced activity was expected to follow the canonical HRF, while those of the TMS- and MNS-induced activity were necessarily not. For all conditions, however, the signal time-course exhibited peaks at 5–6 s, consistent with the standard HRF in all the sampled areas. Furthermore, the analysis of the β2/β1 ratio guaranteed that brain activity could be validly compared across the conditions, by assuming the canonical HRF as a model of hemodynamic changes. Overall, these findings endorsed the validity of results from previous TMS-fMRI studies that assumed the

Table 2D
Results from the group-level statistical parametric mapping analysis. Activity associated with median nerve stimulation at the wrist above the motor threshold (motor-MNS).

Activity clusters (functional anatomy)	Coordinates			T-value
	x	y	z	
Left superior temporal gyrus	−40	−2	−14	9.67
Right rolandic operculum (S2)	48	0	14	8.68
Left insula (S2)	−42	−4	8	7.98
Left superior temporal gyrus (S2)	−50	−34	12	7.95
Left Heschl's gyrus (auditory)	−38	−24	6	7.88
Left SMA (Area 6)	−8	−12	48	7.78
Right superior temporal gyrus	56	−36	18	7.66
Left superior temporal gyrus (S2)	−56	−32	12	7.60
Left postcentral gyrus (S1/M1)	−32	−32	70	7.52
Left superior temporal gyrus (intraparietal sulcus, S2)	−64	−32	22	7.37
Left superior temporal gyrus (auditory)	−54	−14	2	7.31
Right insula (Area 44)	44	12	0	6.89
Right insula (S2)	40	−6	−2	6.84
Left thalamus	−2	−18	−6	6.60
Left M1	−34	−30	66	6.23
Left inferior frontal gyrus (Area 44)	−58	4	14	6.09
Left putamen	−32	−8	−2	6.05
Left middle cingulate cortex (RCZ)	−16	−36	42	5.86
Left STN	−8	−20	−6	5.72
Left temporal pole	−58	6	−10	5.67
Right temporal pole	56	8	−6	5.61
Left postcentral gyrus (S1)	−44	−36	60	5.47
Left paracentral lobule (M1/SMA)	−10	−20	62	5.35

M1 = primary motor cortex, PMd = dorsal premotor cortex, SMA = supplementary motor area, S1 = primary somatosensory cortex, S2 = second somatosensory cortex, RCZ = rostral cingulate zone, S2 = second somatosensory cortex, CCZ = caudal cingulate zone

Table 3A
Results from the group-level statistical parametric mapping with specific contrasts. Suprathreshold TMS relative to subthreshold TMS.

Activity clusters (functional anatomy)	Coordinates			T-value
	x	y	z	
Left M1	−32	−26	62	5.12[†]
Left PMd	−28	−12	62	3.42[*]
Left S1	−30	−28	66	4.26[*]
Left SMA/CCZ	−10	−6	52	3.80[*]
Left putamen	−38	−6	4	3.51[*]

List of areas showing a significant activity in each specific contrast at a threshold of FWE corrected $P<0.05$. M1 = primary motor cortex, PMd = dorsal premotor cortex, SMA = supplementary motor area, S1 = primary somatosensory cortex, CCZ = caudal cingulate zone, STN = subthalamic nucleus.
[*] Significant with a small volume correction analysis.

standard HRF for TMS-induced fMRI changes in both stimulated and remote regions. Hence, it is meaningful to compare the spatial distribution of TMS-induced fMRI responses with those during other motor-related tasks.

The distribution of cortico-cortical evoked activity in the motor network agrees with the previous findings from simultaneous fMRI/PET during TMS applied to M1 (Bestmann et al., 2003; Fox et al., 2006; Hanakawa et al., 2009; Siebner et al., 1998). TMS induced activity in motor areas contralateral to the stimulated hemisphere perhaps through the interhemispheric fiber connection. TMS-induced activity in the right M1 was significant during supra-TMS after the SVC correction. Although the right M1 activity during the sub-TMS did not reach significance in the SPM analysis, the time-course analysis suggested that both supra- and sub-TMS might induce activity in the homologous site in the contralateral hemisphere. This finding might relate to the effects of repetitive TMS onto the homologous region contralateral to the simulation site as previously shown with simultaneous TMS and blood perfusion measurement (Okabe et al., 2003). Concurrent TMS and PET/fMRI studies previously reported hemodynamic activity or dopamine release in the putamen (Hanakawa et al., 2009; Paus et al., 2001; Speer et al., 2003; Strafella et al., 2003) and STN (Strafella et al., 2004). However, relatively little attention has been paid to the potential of cortico-basal ganglia connectivity mapping using TMS-fMRI/PET. In the present study, the posterior putamen and STN showed significant activation during the supra-TMS and a trend toward activation during sub-TMS. The posterolateral putamen constitutes the somatotopically-organized input stage of the basal ganglia-thalamocortical motor circuit (Nambu et al., 2002). The location of the present putaminal activity corresponded to areas involved in hand representation (Gerardin et al., 2003). The STN receives direct inputs from the M1 as well as indirect inputs via the external segment of the

Table 3B
Results from the group-level statistical parametric mapping with specific contrasts. Motor-MNS relative to sensory-MNS.

Activity clusters (functional anatomy)	Coordinates			T-value
	x	y	z	
Left postcentral gyrus (S1, M1)	−28	−32	74	7.91
Left M1	−36	−32	68	5.11[*]
Left S1	−30	−32	72	7.41[*]
Left SMA/CCZ	−8	−14	44	3.96[*]
Left putamen	−32	−14	2	5.04[*]
Left putamen	−26	−12	−2	4.47[*]
Left STN	−12	−20	−2	5.15[*]
Left thalamus	−12	−24	0	5.72[*]

List of areas showing a significant activity in each specific contrast at a threshold of FWE corrected $P<0.05$. M1 = primary motor cortex, PMd = dorsal premotor cortex, SMA = supplementary motor area, S1 = primary somatosensory cortex, CCZ = caudal cingulate zone, STN = subthalamic nucleus.
[*] Significant with a small volume correction analysis.

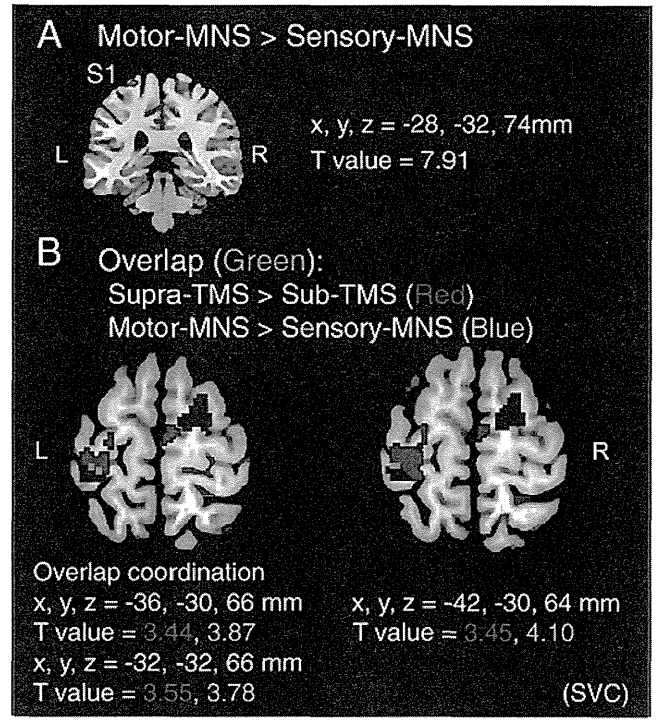

Fig. 6. A: A group-level statistical parametric map showing the categorical comparison of hemodynamic changes between the motor-MNS and sensory-MNS conditions (whole-brain FWE-corrected $P<0.05$). B: Group-level statistical parametric maps comparing the loci of activation between the motor-MNS relative to sensory MNS (blue) and the supra-TMS relative to sub-TMS (red). The threshold is set at uncorrected $P<0.001$ for display purposes. The supra-TMS condition induced activity slightly anterior to that induced by motor-MNS in the left central region (M1 and S1) and in the right premotor areas. The overlap (green) of motor-MNS minus sensory-MNS and Supra-TMS minus Sub-TMS exists in the left precentral and postcentral gyri (M1 and S1).

globus pallidus (Nambu et al., 2002). The importance of STN in human motor control has recently drawn substantial research attention (Aron et al., 2007; Aron and Poldrack, 2006). The present results suggest that functional connectivity mapping of the cortico-basal ganglia pathway may be achieved using simultaneous TMS-fMRI.

We also replicated the findings of earlier studies (Bestmann et al., 2003; Fox et al., 2006; Hanakawa et al., 2009) that both sub-TMS and supra-TMS recruited the remote motor areas such as the SMA whereas only the supra-TMS did the directly stimulated M1. Moreover, the present study supported the idea that muscle afferents inherent to the suprathreshold TMS contributed to activity in the M1 (Bestmann et al., 2003; Fox et al., 2006; Hanakawa et al., 2009; Speer et al., 2003). This idea has been discussed in those studies, but never been directly tested. We found widespread muscle afferent-induced activity in motor areas even though we designed the experiment to minimize their effects. In M1, moderate activity was observed during the motor-MNS that induced muscle twitching, but not during the sensory-MNS. This meant that muscle afferents and/or their perception induced M1 activity because these components are the primary discriminating factor between the motor- and sensory-MNS conditions. Indeed, the close localization of supra-TMS-induced activity (relative to sub-TMS) and motor-MNS induced activity (relative to sensory-MNS) (Fig. 6B) has lent support to the idea that afferent inputs from twitched muscles contribute to brain activity during supra-TMS in M1 (Bestmann et al., 2003; Fox et al., 2006). Moreover, motor-MNS induced activation in the SMA and basal ganglia. This finding meant that muscle afferent-induced activity might even explain activity in the motor network during suprathreshold M1

stimulation, at least in part. Previous research has shown that MNS above the motor threshold can evoke long-latency cortical potentials, but not short-latency potentials, in motor-related areas such as the SMA (Allison et al., 1991). Although wide representations of muscle afferent information in motor-related areas have already been recognized, previous neuroimaging studies have often neglected the contribution of muscle afferents to motor area activity during movement. Here we would like to emphasize that motor area activity during suprathreshold TMS to M1 requires careful interpretation by taking the effects of the muscle afferent into account.

It has been unclear why subthreshold-level TMS applied to M1 significantly induced fMRI signal changes in remote motor areas, but not the directly stimulated M1. Our time-course analysis may provide some insight into this question. Consistent with the results of our earlier study (Hanakawa et al., 2009), the directly stimulated M1 showed mild signal increases even during sub-TMS, but the magnitude of signal changes was smaller than that of remote areas such as SMA. Interestingly, sub-TMS induced a signal undershoot from 10 s after the stimulation events only in M1. Although poststimulus undershoot is a normal component of the standard HRF responses (Buxton et al., 1998; Mandeville and Marota, 1999), we need to explain the reason why that specific condition enhanced the poststimulus undershoot compared with the other conditions. A possibility was that TMS affected neurovascular coupling only in the M1. However, if this were the case, we would expect stronger influences in the supra-TMS condition than the sub-TMS condition. Alternatively, suppression of local neural activity might follow initial neuronal excitation after subthreshold TMS as previously observed during TMS to the visual areas of the cat (Allen et al., 2007). By contrast, undershoot was not evident in remote motor areas during sub-TMS in the present experiment. Differences in the excitatory and inhibitory neural processes between the direct and remote areas could explain why subthreshold TMS to M1 only activates remote motor areas.

A previous NIRS study found significant suppression of deoxyhemoglobin after single-pulse monophasic TMS at intensities that did not evoke muscle contraction (100–140% active motor threshold) (Mochizuki et al., 2006). One of the experimental conditions (90% RMT) in the present study is included in their range of stimulation intensity since 100% RMT roughly corresponds to 130–140% AMT (Khedr et al., 2004; Tergau et al., 1999). Because decreases in deoxyhemoglobin must induce increases in $T2^*$ signals measured with fMRI, their finding is consistent with the initial increase in fMRI signals during 90% RMT condition in the present study. Consistent with the present finding, moreover, one subject (Fig. 4) in Noguchi et al. (Noguchi et al., 2003) showed initial increases followed by an undershoot of oxyhemoglobin concentration during single-pulse subthreshold TMS. The sources of exaggerated undershoot after initial signal increases remain an open question. It would be interesting to combine fMRI and NIRS to measure hemodynamic signals after single-pulse TMS with the same stimulus protocol.

The sound levels of TMS clicks get larger as TMS intensities are increased in the MRI environment. In fact, our previous concurrent TMS-fMRI study reported linearly increasing activity in the auditory cortex as a function of TMS intensities (Hanakawa et al., 2009). TMS-induced sounds may have influenced M1 activity in the present experiment since large sounds transiently suppress M1 excitability (Furubayashi et al., 2000). However, it is disputable if the TMS-induced click sounds significantly influence M1 activity during TMS-fMRI experiments. In contrast to the pattern of activity in the auditory cortex, M1 activity changed abruptly at around the RMT in our previous TMS-fMRI experiment (Hanakawa et al., 2009). Consistently, Hart et al. reported that activity in motor areas did not change in relation to sound levels (Hart et al., 2003). Moreover, to assess the effects of TMS-induced click sounds on M1 activity, we ran a pilot study with the same protocol with the present TMS-fMRI experiment, except that the TMS coil was positioned several centimeters apart from the scalp. In this setup, magnetic fields produced by TMS unlikely affected M1 activity, but the sound levels were very similar. The participants either listened to three different levels of TMS-induced click sounds (120% RMT, 90% AMT and 30% MO) or performed voluntary thumb movement in response to the sounds. We did not observe significant effects of sound levels on M1 activity in either condition. Based on these lines of evidence, it seems less likely that motor area activity in the present experiment was significantly affected by the levels of the click sound produced by TMS. Nevertheless, the effects of click sounds during concurrent TMS-fMRI needs to be addressed formally in the future studies.

In conclusion, the present study provided empirical evidence supporting the use of standard HRF for detecting single-pulse TMS-induced activity in both directly stimulated and remote areas. However, subsequent decreases of fMRI signals after the initial increase (undershoot) were evident only in the directly stimulated M1 during the subthreshold-level TMS condition. The mechanisms underlying this phenomenon should be addressed in future studies. Second, by comparing the distribution of motor area activity among the TMS and the reference conditions, the present experiment for the first time provided evidence that activity ascribed to muscle afferents would contribute to TMS-evoked motor area activity during suprathreshold TMS to M1. A future study should address an issue of how much of the motor area activity results from muscle afferents or TMS-induced neural changes during suprathreshold TMS to M1.

Acknowledgment

The study was supported in part by grants from KAKENHI (20033030 and 20019041) and the Takeda Science Foundation to T.H.

References

Allen, E.A., Pasley, B.N., Duong, T., Freeman, R.D., 2007. Transcranial magnetic stimulation elicits coupled neural and hemodynamic consequences. Science 317, 1918–1921.

Allison, T., McCarthy, G., Wood, C.C., Jones, S.J., 1991. Potentials evoked in human and monkey cerebral cortex by stimulation of the median nerve. A review of scalp and intracranial recordings. Brain 114 (Pt 6), 2465–2503.

Anami, K., Mori, T., Tanaka, F., Kawagoe, Y., Okamoto, J., Yarita, M., Ohmshi, T., Yumoto, M., Matsuda, H., Saitoh, O., 2003. Stepping stone sampling for retrieving artifact-free electroencephalogram during functional magnetic resonance imaging. Neuroimage 19, 281–295.

Aron, A.R., Poldrack, R.A., 2006. Cortical and subcortical contributions to Stop signal response inhibition: role of the subthalamic nucleus. J. Neurosci. 26, 2424–2433.

Aron, A.R., Behrens, T.E., Smith, S., Frank, M.J., Poldrack, R.A., 2007. Triangulating a cognitive control network using diffusion-weighted magnetic resonance imaging (MRI) and functional MRI. J. Neurosci. 27, 3743–3752.

Bestmann, S., Baudewig, J., Siebner, H.R., Rothwell, J.C., Frahm, J., 2003. Subthreshold high-frequency TMS of human primary motor cortex modulates interconnected frontal motor areas as detected by interleaved fMRI-TMS. Neuroimage 20, 1685–1696.

Bestmann, S., Baudewig, J., Siebner, H.R., Rothwell, J.C., Frahm, J., 2004. Functional MRI of the immediate impact of transcranial magnetic stimulation on cortical and subcortical motor circuits. Eur. J. Neurosci. 19, 1950–1962.

Bohning, D.E., Shastri, A., Nahas, Z., Lorberbaum, J.P., Andersen, S.W., Dannels, W.R., Haxthausen, E.U., Vincent, D.J., George, M.S., 1998. Echoplanar BOLD fMRI of brain activation induced by concurrent transcranial magnetic stimulation. Invest. Radiol. 33, 336–340.

Bohning, D.E., Shastri, A., McConnell, K.A., Nahas, Z., Lorberbaum, J.P., Roberts, D.R., Teneback, C., Vincent, D.J., George, M.S., 1999. A combined TMS/fMRI study of intensity-dependent TMS over motor cortex. Biol. Psychiatry 45, 385–394.

Buxton, R., Wong, E., Frank, L., 1998. Dynamics of blood flow and oxygenation changes during brain activation: the balloon model. Magn. Reson. Med. 39, 855–864.

Eickhoff, S.B., Stephan, K.E., Mohlberg, H., Grefkes, C., Fink, G.R., Amunts, K., Zilles, K., 2005. A new SPM toolbox for combining probabilistic cytoarchitectonic maps and functional imaging data. Neuroimage 25, 1325–1335.

Fox, P.T., Narayana, S., Tandon, N., Fox, S.P., Sandoval, H., Kochunov, P., Capaday, C., Lancaster, J.L., 2006. Intensity modulation of TMS-induced cortical excitation: primary motor cortex. Hum. Brain Mapp. 27, 478–487.

Furubayashi, T., Ugawa, Y., Terao, Y., Hanajima, R., Sakai, K., Machii, K., Mochizuki, H., Shiio, Y., Uesugi, H., Enomoto, H., Kanazawa, I., 2000. The human hand motor area is transiently suppressed by an unexpected auditory stimulus. Clin. Neurophysiol. 111, 178–183.

Gerardin, E., Lehericy, S., Pochon, J.B., Tezenas du Montcel, S., Mangin, J.F., Poupon, F., Agid, Y., Le Bihan, D., Marsault, C., 2003. Foot, hand, face and eye representation in the human striatum. Cereb. Cortex 13, 162–169.

Hanakawa, T., Mima, T., Matsumoto, R., Abe, M., Inouchi, M., Urayama, S., Anami, K., Honda, M., Fukuyama, H., 2009. Stimulus–response profile during single-pulse transcranial magnetic stimulation to the primary motor cortex. Cereb. Cortex 19, 2605–2615.

Hart, H.C., Hall, D.A., Palmer, A.R., 2003. The sound-level-dependent growth in the extent of fMRI activation in Heschl's gyrus is different for low- and high-frequency tones. Hear. Res. 179, 104–112.

Henson, R.N., Price, C.J., Rugg, M.D., Turner, R., Friston, K.J., 2002. Detecting latency differences in event-related BOLD responses: application to words versus nonwords and initial versus repeated face presentations. NeuroImage 15, 83–97.

Khedr, E.M., Gilio, F., Rothwell, J., 2004. Effects of low frequency and low intensity repetitive paired pulse stimulation of the primary motor cortex. Clin. Neurophysiol. 115, 1259–1263.

Logothetis, N., 2000. Can current fMRI techniques reveal the micro-architecture of cortex? Nat. Neurosci. 3, 413–414.

Mandeville, J., Marota, J., 1999. Vascular filters of functional MRI: spatial localization using BOLD and CBV contrast. Magn. Reson. Med. 42, 591–598.

Mochizuki, H., Ugawa, Y., Terao, Y., Sakai, K.L., 2006. Cortical hemoglobin-concentration changes under the coil induced by single-pulse TMS in humans: a simultaneous recording with near-infrared spectroscopy. Exp. Brain Res. 169, 302–310.

Nair, D., 2005. About being BOLD. Brain Res. Brain Res. Rev. 50, 229–243.

Nambu, A., Kaneda, K., Tokuno, H., Takada, M., 2002. Organization of corticostriatal motor inputs in monkey putamen. J. Neurophysiol. 88, 1830–1842.

Noguchi, Y., Watanabe, E., Sakai, K.L., 2003. An event-related optical topography study of cortical activation induced by single-pulse transcranial magnetic stimulation. NeuroImage 19, 156–162.

Ogawa, S., Lee, T., Stepnoski, R., Chen, W., Zhu, X., Ugurbil, K., 2000. An approach to probe some neural systems interaction by functional MRI at neural time scale down to milliseconds. Proc. Natl. Acad. Sci. U. S. A. 97, 11026–11031.

Okabe, S., Hanajima, R., Ohmshi, T., Nishikawa, M., Imabayashi, E., Takano, H., Kawachi, T., Matsuda, H., Shiio, Y., Iwata, N.K., Furubayashi, T., Terao, Y., Ugawa, Y., 2003. Functional connectivity revealed by single-photon emission computed tomography (SPECT) during repetitive transcranial magnetic stimulation (rTMS) of the motor cortex. Clin. Neurophysiol. 114, 450–457.

Paus, T., Jech, R., Thompson, C.J., Comeau, R., Peters, T., Evans, A.C., 1997. Transcranial magnetic stimulation during positron emission tomography: a new method for studying connectivity of the human cerebral cortex. J. Neurosci. 17, 3178–3184.

Paus, T., Sipila, P.K., Strafella, A.P., 2001. Synchronization of neuronal activity in the human primary motor cortex by transcranial magnetic stimulation: an EEG study. J. Neurophysiol. 86, 1983–1990.

Rollnik, J., Düsterhoft, A., Dauper, J., Kossev, A., Weissenborn, K., Dengler, R., 2002. Decrease of middle cerebral artery blood flow velocity after low-frequency repetitive transcranial magnetic stimulation of the dorsolateral prefrontal cortex. Clin. Neurophysiol. 113, 951–955.

Rossini, P.M., Barker, A.T., Berardelli, A., Caramia, M.D., Caruso, G., Cracco, R.Q., Dimitrijevic, M.R., Hallett, M., Katayama, Y., Lucking, C.H., et al., 1994. Non-invasive electrical and magnetic stimulation of the brain, spinal cord and roots: basic principles and procedures for routine clinical application. Report of an IFCN committee. Electroencephalogr. Clin. Neurophysiol. 91, 79–92.

Sallustio, F., Di Legge, S., Rizzato, B., Stanzione, P., Koch, G., 2010. Changes in cerebrovascular reactivity following low-frequency repetitive transcranial magnetic stimulation. J. Neurol. Sci. 295, 58–61.

Siebner, H.R., Willoch, F., Peller, M., Auer, C., Boecker, H., Conrad, B., Bartenstein, P., 1998. Imaging brain activation induced by long trains of repetitive transcranial magnetic stimulation. Neuroreport 9, 943–948.

Speer, A.M., Willis, M.W., Herscovitch, P., Daube-Witherspoon, M., Shelton, J.R., Benson, B.E., Post, R.M., Wassermann, E.M., 2003. Intensity-dependent regional cerebral blood flow during 1-Hz repetitive transcranial magnetic stimulation (rTMS) in healthy volunteers studied with H2150 positron emission tomography: I. Effects of primary motor cortex rTMS. Biol. Psychiatry 54, 818–825.

Strafella, A.P., Paus, T., Fraraccio, M., Dagher, A., 2003. Striatal dopamine release induced by repetitive transcranial magnetic stimulation of the human motor cortex. Brain 126, 2609–2615.

Strafella, A., Vanderwerf, Y., Sadikot, A., 2004. Transcranial magnetic stimulation of the human motor cortex influences the neuronal activity of subthalamic nucleus. Eur. J. Neurosci. 20, 2245–2249.

Tergau, F., Wanschura, V., Canelo, M., Wischer, S., Wassermann, E.M., Ziemann, U., Paulus, W., 1999. Complete suppression of voluntary motor drive during the silent period after transcranial magnetic stimulation. Exp. Brain Res. 124, 447–454.

Wang, J., Li, L., Roc, A., Alsop, D., Tang, K., Butler, N., Schnall, M., Detre, J., 2004. Reduced susceptibility effects in perfusion fMRI with single-shot spin-echo EPI acquisitions at 1.5 Tesla. Magn. Reson. Imaging 22, 1–7.

Yousry, T.A., Schmid, U.D., Alkadhi, H., Schmidt, D., Peraud, A., Buettner, A., Winkler, P., 1997. Localization of the motor hand area to a knob on the precentral gyrus. A new landmark. Brain 120 (Pt 1), 141–157.

Zhang, D., Snyder, A.Z., Fox, M.D., Sansbury, M.W., Shimony, J.S., Raichle, M.E., 2008. Intrinsic functional relations between human cerebral cortex and thalamus. J. Neurophysiol. 100, 1740–1748.

Zonta, M., Angulo, M., Gobbo, S., Rosengarten, B., Hossmann, K., Pozzan, T., Carmignoto, G., 2003. Neuron-to-astrocyte signaling is central to the dynamic control of brain microcirculation. Nat. Neurosci. 6, 43–50.

NeuroImage 59 (2012) 4006–4021

Contents lists available at SciVerse ScienceDirect

NeuroImage

journal homepage: www.elsevier.com/locate/ynimg

Cortical current source estimation from electroencephalography in combination with near-infrared spectroscopy as a hierarchical prior

Takatsugu Aihara [a], Yusuke Takeda [b], Kotaro Takeda [a,c], Wataru Yasuda [a], Takanori Sato [a,d], Yohei Otaka [e], Takashi Hanakawa [f], Manabu Honda [f], Meigen Liu [g], Mitsuo Kawato [a], Masa-aki Sato [b,*], Rieko Osu [a]

[a] ATR Computational Neuroscience Laboratories, Kyoto 619-0288, Japan
[b] ATR Neural Information Analysis Laboratories, Kyoto 619-0288, Japan
[c] Clinical Research Center, National Hospital Organization Murayama Medical Center, Tokyo 208-0011, Japan
[d] Department of Electrical, Electronics and Information Engineering Faculty of Engineering, Nagaoka University of Technology, Niigata 940-2188, Japan
[e] Tokyo Bay Rehabilitation Hospital, Chiba 275-0026, Japan
[f] National Institute of Neuroscience, National Center of Neurology and Psychiatry, Tokyo 187-8502, Japan
[g] Department of Rehabilitation Medicine, Keio University, Tokyo 160-8582, Japan

ARTICLE INFO

Article history:
Received 28 April 2011
Revised 26 September 2011
Accepted 30 September 2011
Available online 14 October 2011

Keywords:
Variational Bayesian Multimodal EncephaloGraphy (VBMEG)
Electroencephalography (EEG)
Near-infrared spectroscopy (NIRS)

ABSTRACT

Previous simulation and experimental studies have demonstrated that the application of Variational Bayesian Multimodal EncephaloGraphy (VBMEG) to magnetoencephalography (MEG) data can be used to estimate cortical currents with high spatio-temporal resolution, by incorporating functional magnetic resonance imaging (fMRI) activity as a hierarchical prior. However, the use of combined MEG and fMRI is restricted by the high costs involved, a lack of portability and high sensitivity to body-motion artifacts. One possible solution for overcoming these limitations is to use a combination of electroencephalography (EEG) and near-infrared spectroscopy (NIRS). This study therefore aimed to extend the possible applications of VBMEG to include EEG data with NIRS activity as a hierarchical prior. Using computer simulations and real experimental data, we evaluated the performance of VBMEG applied to EEG data under different conditions, including different numbers of EEG sensors and different prior information. The results suggest that VBMEG with NIRS prior performs well, even with as few as 19 EEG sensors. These findings indicate the potential value of clinically applying VBMEG using a combination of EEG and NIRS.

Introduction

Magnetoencephalography (MEG) and electroencephalography (EEG) provide direct measures of the magnetic and electrical fields caused by neural activity, respectively, with high temporal resolution. The spatial resolution of these techniques, however, is relatively poor, because MEG/EEG signals measured on the scalp surface are comprised of a mixture of signals originating from a large number of cortical areas. Because many different source configurations can generate the same distribution of magnetic/electric fields on the scalp, it is necessary to solve an ill-posed inverse problem to improve the spatial resolution (Michel, et al., 2004). Inverse procedures are commonly classified as dipole and distributed source methods. Dipole methods (Hari, 1991; Mosher et al., 1992) solve the inverse problem by approximating brain activity using a small number of current dipoles. Although the methods provide good estimates when the number of active areas is small, it is difficult to determine the appropriate number of dipole sources for complicated spatio-temporal activity. In addition, neural current distribution over the cortical surface cannot be estimated by dipole methods. On the other hand, distributed methods assume a large number of current dipoles distributed in the brain (Hamalainen et al., 1993). In a linear approach to resolving the inverse problem, several prior assumptions can be used such as the minimum norm method. Unfortunately, the prior assumptions are insufficient to fully resolve the ill-posed nature of the inverse problem, meaning that the spatial resolution of these methods is still rather low. Attempts have been made to overcome these limitations using functional information obtained with other imaging modalities, such as functional magnetic resonance imaging (fMRI) (for a review of EEG–fMRI integration, see Rosa et al., 2010). These approaches, such as the Wiener filter or the Bayesian method (Dale et al., 2000; Kajihara et al., 2004; Phillips et al., 2002; Schmidt et al., 1999), use fMRI data as prior information on the source current variance by assuming that the current variances for fMRI-active dipoles are large compared with those for fMRI-inactive dipoles. However, source current estimation based on these methods may fail if the fMRI data contain incorrect information. In recent years, there are several attempts to overcome these difficulties (Daunizeau et al., 2005; Grova et al., 2008; Henson et al., 2010).

* Corresponding author at: 2-2-2 Hikaridai, Keihanna Science City, Kyoto 619-0288, Japan. Fax: +81 774 95 1259.
E-mail address: masa-aki@atr.jp (M. Sato).

1053-8119/$ – see front matter © 2011 Elsevier Inc. All rights reserved.
doi:10.1016/j.neuroimage.2011.09.087

We previously proposed Variational Bayesian Multimodal EncephaloGraphy (VBMEG) as a hierarchical Bayesian estimation method that incorporates fMRI activity information as a hierarchical prior to overcome the vulnerability to inaccuracies in fMRI information (Sato et al., 2004). In this method, the variance of the source current at each source location is considered to be an unknown parameter and is estimated from the observed MEG data and prior information. The fMRI information can be imposed as prior information on the variance distribution rather than the variance itself, such that it places a soft constraint on the variance. Combined MEG and fMRI measurements confirmed that VBMEG could be used to estimate brain activity with high spatio-temporal resolution in both computer simulations (Sato et al., 2004) and real experiments involving visual (Yoshioka et al., 2008) and motor tasks (Toda et al., 2011).

We have been postulating that VBMEG with a combination of MEG and fMRI can make a substantial contribution to neuroscience research. However, studies combining MEG and fMRI are limited by the high sensitivity of these methods to body-motion artifacts, a lack of portability, and high costs. Some or all of these factors reduce the suitability of this combined method for measuring brain activity in infants or patients, for investigating brain activity related to human motor control in realistic situations (e.g., in sitting or standing positions), and for daily use, e.g., monitoring day-to-day changes in brain activities during stroke recovery or motor learning. One possible solution for overcoming these limitations is to use a combination of EEG and NIRS, rather than MEG and fMRI. The reasoning behind this approach is that both EEG and MEG record brain electrical activity, whereas fMRI and NIRS measure blood-flow-related signals in the brain. EEG and NIRS have lower sensitivity to body-motion artifacts, higher portability and lower costs, compared to MEG/fMRI. We therefore applied VBMEG to EEG data by incorporating NIRS activity as a hierarchical prior.

In the present study, we initially conducted computer simulations to investigate the performance of VBMEG applied to EEG data. VBMEG was applied to simulated EEG data with different types of prior information (no prior, correct prior and incorrect prior) to investigate the effects of prior information on estimation accuracy. The effects of the resolution of prior information on estimation accuracy were also investigated because the different imaging modalities, providing prior information, have different spatial resolutions. In addition, the effects of the number of EEG sensors on estimation accuracy were investigated, because the use of fewer sensors is advantageous from the subject's point of view, particularly for infants and patients.

We then conducted real experiments in subjects performing a motor task and applied VBMEG to real EEG data to confirm the results of the computer simulations. We compared the performance of VBMEG with fMRI prior, NIRS prior and no prior, and investigated the effects of the number of EEG sensors for both fMRI and NIRS priors.

A motor task was used for the following reasons. First, brain activity associated with movement, especially with the preparation and execution of movements, has been well studied. Regarding the spatial patterns of motor-related brain activity, the existence of laterality and somatotopy in the sensorimotor area is well known; for example, right finger movements activate the hand area of the contralateral (i.e., left) sensorimotor area. Regarding the temporal pattern of brain activity for voluntary movements, movement-related potentials (MRPs) recorded using EEG are known to be divided into three subcomponents: (1) the Bereitschaftspotential (BP), a slowly rising negative component starting 1000–1500 ms before electromyography (EMG) onset; (2) the negative slope (NS), a steeper increase in negativity starting around 400 ms before EMG onset; and (3) the motor potential (MP), a further increase in negativity appearing around EMG onset and peaking just after EMG onset. The earliest component, the BP, shows widespread and symmetrical scalp distribution, suggesting that it may reflect cortical activity related to early movement preparation, arising predominantly from the supplementary motor area (SMA). In contrast, the later components, the NS and MP, show clear lateralization towards the hemisphere contralateral to the movement, suggesting that the NS and MP reflect cortical activity associated with late preparation and execution, arising predominantly from the contralateral primary motor area (M1) (Cunnington et al., 1996). Second, as described previously, we propose that VBMEG with a combination of EEG and NIRS can provide a suitable approach for monitoring day-to-day changes in brain activity during recovery of motor function after stroke. One of the aims of the present study was therefore to lay the foundations for such future studies.

The motor task in the present study was a repetitive right-finger movement task. The movement repetition rate was slow (less than 0.3 Hz) in the EEG experiments, which were conducted using an event-related design, and rapid (as fast as possible) in both the fMRI and NIRS experiments, which were conducted using a block design. Previous studies have reported that the primary sensorimotor areas (SM1) and SMA are activated during slow-rate movements, reflecting not only the execution and somatosensory information processing stages, but also the preparation stage, whereas SM1 is predominantly activated during fast-rate movements, mainly reflecting the late preparation, execution and somatosensory information processing stages (Kunieda et al., 2000; Toma et al., 1999). Brain activity of the late preparation, execution and somatosensory information processing stages (i.e., SM1 activity) is thus commonly observed during both movements. The present study therefore focused on these stages.

Materials and methods

Computer simulations

Computer simulations were conducted to investigate the performance of VBMEG applied to EEG data.

Simulated EEG data

A polygon model of cortical surfaces (20,004 vertex points) was constructed from a T1 structural image (for MRI data, see MRI experiments and analysis) of an experimental subject (RO) using FreeSurfer software (Dale et al., 1999). A single current dipole was assumed at each vertex point perpendicular to the cortical surface. The brain structures were approximated as a three-layer model by identifying three boundaries, for the cerebrospinal fluid (CSF), skull and scalp. These surfaces obtained by FreeSurfer were slightly modified using gray/white/CSF segmentation by SPM2 (Welcome Department of Cognitive Neurology, UK) and morphological operations. This MRI-based three-layer model was used in the following simulations to calculate a lead field, which converts cortical currents to EEG data. We assumed that the conductivities of the CSF, skull and scalp were 0.33, 0.0042, and 0.33 S/m (Waberski, et al., 1998), respectively.

We assumed two single dipole sources (S_1 and S_2), both located at a cortical vertex that was randomly selected from 20,004 vertices. The waveform of every source current was the product of a sinusoidal wave (4-Hz for S_1 and 10-Hz for S_2) and Hanning window. Both sources became active at 0 ms, peaked at 200 ms (peak amplitudes 10-nAm), and returned to the baseline level at 400 ms. We tested 500 different pairs of S_1 and S_2.

We assumed that every cortical dipole exhibits background activity, which is assumed to be independent among dipoles. The background activity was assumed to be a Gaussian white noise with zero mean and standard deviation (SD) 0.2-nAm (1/50 of the peak amplitude of the source current).

We assumed that the head was surrounded by 64, 31, or 19 EEG sensors (Fig. 1) whose positions were determined based on real experimental sensor-position data from the subject (for the position of EEG sensors, see EEG experiments and preprocessing). Simulated

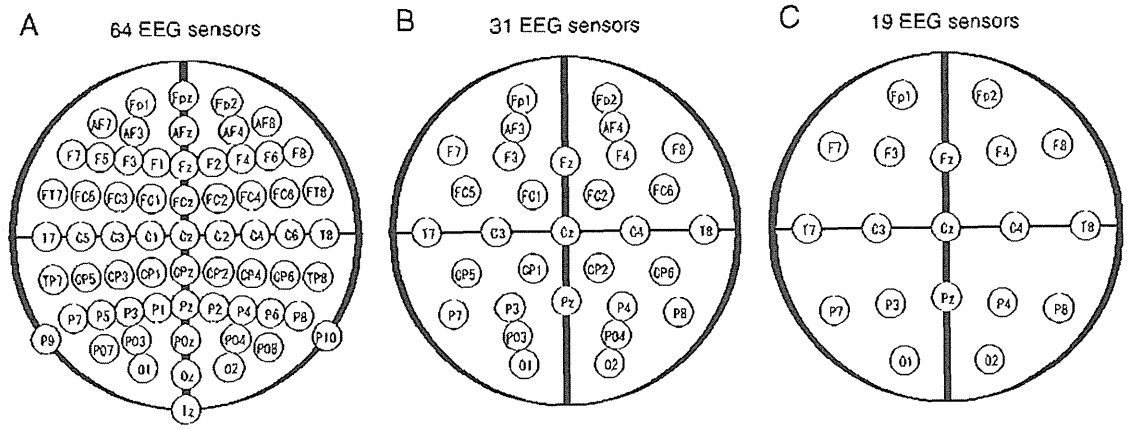

Fig. 1. Placement of EEG sensors according to the International 10–20 system. (A) 64 sensors. (B) 31 sensors. (C) 19 sensors. The positions of these sensors in the simulations were determined on the basis of real experimental data.

EEG data were generated using the forward model (see Eq. (1) in Appendix A). We assumed that every EEG sensor has sensor noise, which was assumed to be independent among sensors. The sensor noise was assumed to be a Gaussian white noise with zero mean and SD of 1.5 μV. Signal to noise ratio (SNR) can be defined as:

$$SNR = S/\sqrt{N_{bg}^2 + N_{sn}^2},$$

where S is the maximum amplitude of EEG originated from cortical source activities, N_{bg} is the variance of EEG originated from cortical background activities, and N_{sn} is the variance of sensor noise. In the above settings of source current amplitude, background activity intensity, and sensor noise level, SNR was 0.81, averaged over 500 source pairs. This value is similar to the SNR obtained in the experimental data described below.

Variational Bayesian Multimodal EncephaloGraphy (VBMEG)

In VBMEG, the prior current variance is considered as a random variable and a hierarchical prior distribution for the prior current variance is introduced (see Appendix A for details of estimation). The activity information, such as that derived from fMRI/NIRS, is imposed not on the current variance itself, but on the hierarchical prior distribution for the current variance through two hyper-parameters: the variance magnification parameter ($m_0 \geq 1$) and the confidence parameter ($\gamma_0 \geq 0$). The magnification parameter (m_0) controls the relative amplitude of the prior current variance; large m_0 increases the prior current variance, especially for dipoles with large activities (i.e., large t-values in the case of fMRI prior) and encourages the estimated current amplitude to increase. The m_0 can be theoretically derived if both the source and background currents are known. In the setting described in Simulated EEG data, m_0 is 674 in theory. The confidence parameter (γ_0) controls the width of the prior distribution and the variance of the prior distribution is inversely proportional to γ_0; large γ_0 narrows the prior distribution around the mean value, and the estimation depends more critically on the activity data. Thus, the activity information can give a soft constraint on the current variance (for details of VBMEG, see Sato et al., 2004; Yoshioka et al., 2008).

Related work in multimodal fusion (e.g., Grova et al., 2008) has reported that a major issue arises in imposing prior constraints on the EEG/MEG inverse problem when the prior information[1] is 'wrong' or distorted, because of false positive or missing sources. In addition, VBMEG is sensitive to the values of hyper-parameters (Yoshioka et al., 2008). Therefore, the first step of the simulations was to investigate the effects of the types of prior information, the values of hyper-parameters, and their interactions on the estimation accuracy, with both the resolution of the prior information and the number of EEG sensors fixed. We used four different types of prior information; no prior, missing prior, correct prior, and false positive prior. The 'no prior'[2] condition indicates that $V_n = 1$ for all dipoles (i.e., uniform spatial prior), where V_n is the prior value at the n-th vertex. The 'correct prior' condition indicates that $V_n = 1$ for dipoles within R-mm radius around both source dipoles (i.e., S_1 and S_2), and $V_n = 0$ for other dipoles. The 'false positive prior' condition indicates that $V_n = 1$ for dipoles within R-mm radius around S_1, S_2 and a randomly selected dipole, and $V_n = 0$ for other dipoles. The 'missing prior' condition indicates that $V_n = 1$ for dipoles within R-mm radius around only S_1, and $V_n = 0$ for other dipoles. This imposes false negative information on the active source, S_2. The value of R corresponds to the spatial resolution of the prior information; the smaller the R value, the higher the spatial resolution. Three different values were used for each hyper-parameter: $m_0 = 1$, 100, 1000, and $\gamma_0 = 1$, 10, 1000. Thus, nine combinations of hyper-parameters were tested. Here, the resolution of the prior information, R, was fixed to six, roughly corresponding to the resolution of the fMRI scanning. The number of EEG sensors was fixed to the maximum value of 64.

In the second step, we investigated the effects of spatial resolution of prior information, the number of EEG sensors, and their interactions on estimation accuracy. The following values of R were used: $R = 6$, 12, and 18. The larger value of R may correspond to the case of NIRS prior, because the spatial resolution of NIRS is worse than that of fMRI. The numbers of EEG sensors were 64, 31, and 19. Here, hyper-parameters were fixed to the following values: $m_0 = 100$ and $\gamma_0 = 10$, according to the result of the first step of the present simulation study. The type of prior was 'correct prior'.

Evaluation of estimation accuracy

In the first step of the simulation, we used four evaluation metrics to access the performance of VBMEG.

The first metric, the area under curve (AUC), is based on the receiver operating characteristic (ROC) curve approach (Daunizeau, et al., 2005; Grova et al., 2006, 2008; Ou et al., 2010). For each combination of true sources, the AUC was calculated in the following way. Normalized energy for the estimated current distribution for the k-th dipole was defined as: $E_{estimated}(k) = \left\| Z^k_{estimated} \right\|^2 / \max_k \left(\left\| Z^k_{estimated} \right\|^2 \right)$, where

[1] Throughout this paper, 'prior information' refers to prior functional or activity information, because we were only interested in the effects of functional (activity) information. Note that VBMEG incorporates both structural and functional (activity) information as priors.

[2] Throughout this paper, 'no prior' indicates that no functional MRI/NIRS information was used as a hierarchical prior. Note that structural MRI information, however, was incorporated as a prior in these cases.

$Z^k_{estimated}$ is the estimated current averaged around peak time (195–205 ms; it should be noted that both S_1 and S_2 reach peak at 200 ms) of the k-th dipole. On the other hand, normalized energy for the true current distribution for the k-th dipole, $E_{true}(k)$, was defined as: $E_{true}(k)=1$ if the distance between the k-th dipole and S_1 or S_2 was less than R-mm (it should be noted that R is the resolution of prior information), and $E_{true}(k)=0$ otherwise. For a threshold β chosen in the interval [0, 1] (to be precise, $\beta=1.2^{-200}, 1.2^{-199}, \ldots, 1.2^{-2}, 1.2^{-1}$), we considered the k-th dipole to be active if its energy $E_{estimated}(k)\geq\beta$. By comparing the estimated energy, $E_{estimated}(k)$, with the true energy, $E_{true}(k)$, for each dipole, we were able to quantify the amount of true positive (TP), true negative (TN), false positive (FP) and false negative (FN) for each threshold β. Sensitivity and specificity were then estimated as follows:

$$sensitivity(\beta)=\frac{TP(\beta)}{TP(\beta)+FN(\beta)},\text{ and }\quad specificity(\beta)=\frac{TN(\beta)}{TN(\beta)+FP(\beta)}.$$

ROC curves were then obtained by plotting sensitivity (β) against (1-specificity(β)) for different thresholds β. The area under the ROC curve (AUC), a well-known criterion to assess detection accuracy, was then calculated according to the trapezium rule. An AUC value of 1 indicates the perfect detection performance and lower values indicate lower performance. Potential biases of specificity estimation (due to the imbalance between the active and the inactive dipoles) were corrected as in Grova et al. (2006) (see Appendix B for the method of the bias correction). The AUCs for S_1 and S_2 were averaged across 500 combinations of sources.

The second metric was the correlation coefficient (R_{st}) between spatio-temporal patterns of the true and estimated currents, calculated across the whole activated duration (400 ms):

$$\left\langle\overline{Z_{true}}\right\rangle=\frac{1}{T}\sum_t\frac{1}{K}\sum_k Z^k_{true}(t),\quad \left\langle\overline{Z_{estimated}}\right\rangle=\frac{1}{T}\sum_t\frac{1}{K}\sum_k Z^k_{estimated}(t),$$

$$R_{st}=\frac{\sum_t\sum_k\left\{Z^k_{true}(t)-\left\langle\overline{Z_{true}}\right\rangle\right\}\cdot\left\{Z^k_{estimated}(t)-\left\langle\overline{Z_{estimated}}\right\rangle\right\}}{\sqrt{\sum_t\sum_k\left\{Z^k_{true}(t)-\left\langle\overline{Z_{true}}\right\rangle\right\}^2}\cdot\sqrt{\sum_t\sum_k\left\{Z^k_{estimated}(t)-\left\langle\overline{Z_{estimated}}\right\rangle\right\}^2}},$$

where T is the number of time points in the analysis window (400 ms in this case), K is the number of cortical dipoles (20,004 in this case), $Z^k_{true}(t)$ is the true current at the k-th dipole and time t, and $Z^k_{estimated}(t)$ is the estimated current at the k-th dipole and time t. This metric tests whether the spatio-temporal pattern of the estimated currents is similar to that of the true currents.

The third metric was the correlation coefficient (R_s) between spatial patterns of the true and estimated currents averaged around peak time (195–205 ms):

$$\overline{Z_{true}}=\frac{1}{K}\sum_k Z^k_{true},\quad \overline{Z_{estimated}}=\frac{1}{K}\sum_k Z^k_{estimated},$$

$$R_s=\frac{\sum_k\left(Z^k_{true}-\overline{Z_{true}}\right)\cdot\left(Z^k_{estimated}-\overline{Z_{estimated}}\right)}{\sqrt{\sum_k\left(Z^k_{true}-\overline{Z_{true}}\right)^2}\cdot\sqrt{\sum_k\left(Z^k_{estimated}-\overline{Z_{estimated}}\right)^2}},$$

where Z^k_{true} and $Z^k_{estimated}$ are the temporal averages (around peak time; 195–205 ms) of the true and estimated currents, respectively. This metric shows whether the spatial pattern of the estimated currents is similar to that of the true currents.

The fourth metric was the root mean squared error (RMSE) to assess the accuracy of estimation of the current amplitude over the all dipoles (Daunizeau et al., 2005):

$$RMSE=\sqrt{\frac{1}{T}\sum_t\frac{1}{K}\sum_k\left(Z^k_{true}(t)-Z^k_{estimated}(t)\right)^2}.$$

This was also calculated across the whole activated duration (400 ms).

In the second step of the simulation, we applied the four metrics used in the first step. In addition, we used localization error and estimation gain as two other metrics. The former reflects the precision of the source localization and the latter reflects the accuracy of the amplitude estimation at the source position. For each dipole, amplitude was averaged around peak time (195–205 ms). Localization error was defined as the distance between true and estimated sources, where the estimated source was the dipole that had the maximum of the averaged amplitude. For both true and estimated sources, we calculated the sum of the averaged amplitudes from dipoles within a 6 mm radius around the source. Estimation gain was defined as the ratio of the sum of the averaged amplitudes between true and estimated sources.

Application of VBMEG to real EEG data

We conducted experiments to confirm whether the findings obtained in the simulation study were applicable to real experimental data. We investigated performance of VBMEG with different types of prior information (fMRI prior, NIRS prior and no prior) and different numbers of EEG sensors (64, 31 and 19).

Subjects

Two subjects (TA and RO; aged 32–41, one male and one female) took part in the fMRI, NIRS and EEG experiments. Both subjects gave written informed consent for the experimental procedures, which were approved by the ATR Human Subject Review Committee.

MRI experiments and analysis

Structural and functional MRI data were recorded using a 3T Magnetom Trio MRI scanner (Siemens, Munich, Germany). The acquisition parameters for T1-weighted images were as follows: repetition time 2 s, time of echo 4.38 ms, flip angle 8°, slice thickness 1 mm, field of view 256×256 mm, imaging matrix 256×256 and 208 slices. The acquisition parameters for echo-planar images (EPIs) were as follows: repetition time 3 s, time of echo 30 ms, flip angle 60°, slice thickness 3 mm, field of view 192×192 mm, imaging matrix 64×64 mm and 44 slices.

The fMRI experiments consisted of alternating blocks of rest and task periods (18 s each). During a rest period, the word 'rest' was presented at the center of the display and subjects remained quiet. During a task period, subjects conducted repetitive movements of the right index finger (brisk extension and flexion at the metacarpophalangeal joints) as fast as possible, according to the instruction 'right index finger' presented at the center of the display. There were eight (subject RO) or nine (subject TA) blocks.

A polygon cerebral cortex model was constructed for each subject using FreeSurfer software (Dale et al., 1999) from the T1 structural image of the subject. The number of vertices for each subject was 20,004. A single current dipole was assumed at each vertex point perpendicular to the cortical surface. For the calculation of the lead field, the brain structures were approximated as a three-layer model by identifying three boundaries, for CSF, skull and scalp. These surfaces obtained by FreeSurfer were slightly modified using gray/white/CSF segmentation by SPM2 and morphological operations. This MRI-based three-layer model was used as a forward model, describing the relationship between cortical currents and EEG data, in the following analysis for source current estimation from EEG using VBMEG. The conductivities of the CSF, skull and scalp used in the analysis of real data were the same as those used in the simulations.

fMRI signals elicited by the movements were analyzed using SPM2 to obtain prior information on the variances of the cortical currents. Head motion was corrected and the images were smoothed using an 8-mm full-width at half maximum (FWHM) Gaussian filter. The

voxel t-values were calculated for the difference between the task and rest periods. The resulting t-values were thresholded ($p<0.001$, uncorrected for multiple comparisons), normalized to have a maximum value of 1, then mapped to the cortical vertices for the prior information of source current estimation, as described previously (Fujiwara et al., 2009; Toda et al., 2011; Yoshioka et al., 2008).

NIRS experiments and analysis

Subjects were seated in a comfortable reclining armchair. NIRS recording was performed using an optical imaging system (FOIRE-3000, Shimadzu Co., Japan). Bilateral SM1, bilateral SMA, and bilateral dorsal premotor area (PMA) were covered with 16 emitters and 12 detectors which provided 43-channel recording of changes in the concentrations of oxygenated hemoglobin and deoxygenated hemoglobin (Δ[OxyHb] and Δ[DeoxyHb], respectively). For the 43-channel recording, each distance between one emitter and one detector was set at 3 cm (long distance channel: long-ch). To reduce artifacts related to skin blood flow, four short-distance (1.5 cm) source-detector channels (short distance channel: short-ch) were also placed onto the bilateral frontal and parietal lobes (Fig. 2). It should be noted that signals measured from short distance channels mainly originated from surface tissues (Okada et al., 1997).

The NIRS experiments consisted of alternating blocks of rest–task–rest periods (15 s each). The start of the task period was indicated by a single click sound, while the end was indicated by two clicks. During a rest period, subjects were presented with a fixation point and remained quiet. During a task period, subjects performed repetitive movements of the right index finger (the same as those in the fMRI experiment) as rapidly as possible. Each session consisted of six blocks.

After the NIRS experiment, probe positions were measured using a stylus marker (FASTRAK; Polhemus, U.S.A.) to allow subsequent co-registration of EEG and NIRS results.

Three near-infrared beams (wavelengths 780, 805, and 830 nm) were irradiated and detection beams sampled every 130 ms were used to calculate Δ[OxyHb] and Δ[DeoxyHb]. The present study focused on Δ[OxyHb] because it is a more sensitive parameter of cerebral blood flow (Hoshi et al., 2001; Strangman et al., 2002). In each long-distance recording channel (43 channels), the time-series data for Δ[OxyHb] were smoothed using a Gaussian kernel of 4 s FWHM. The baseline trend for Δ[OxyHb] in each task block was then removed using linear-fitting to the signals of baseline intervals (10 s rest period just before the task onset and 5 s rest period after 10 s of the task offset). To normalize the amplitude of Δ[OxyHb], the smoothed and trend-reduced data were transformed to z-score values using the SD during rest periods in the rest blocks (10 s before the task and 5 s after 10 s of the task).

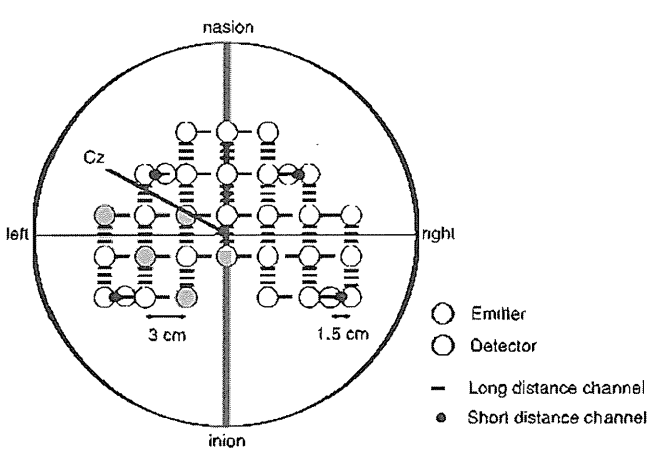

Fig. 2. NIRS probe positions. Emitters and detectors are indicated by gray and white circles, respectively. Long- and short-distance channels are shown by dotted lines and black points, respectively.

The following process was used to remove the skin blood flow artifacts from long-ch data. The four short-ch data were normalized to z-scores using the same process as for long-ch. Principal component analysis (PCA) was used to estimate the skin blood flow artifact. In this study, we considered the first component to represent this artifact. We computed multiple regression coefficients on the basis of a model in which data from long-ch was modeled as a linear sum of hemodynamic response function, skin blood flow artifact (the first principal component) and a constant. We then subtracted the artifact and bias components from the long-ch data to produce artifact-free Δ[OxyHb] data.

For the long-ch data, the peak value of the artifact-free Δ[OxyHb] during the task period was regarded as NIRS activity. The NIRS activity was normalized by dividing the peak value in each channel by the maximum value of the 43 channels. The normalized NIRS activity was mapped onto the cerebral cortex using Fusion software (Shimadzu Co., Japan) for the prior information of VBMEG, according to the following method. First, the position of the every probe was superimposed on the model of the scalp, and the position of every NIRS channel was estimated as the center point between the corresponding emitter and detector. Second, the cortical projection point of each NIRS channel position was determined according to the method described by Okamoto et al. (2004) (see Appendix C). Third, the normalized activity data for each NIRS channel was applied to cortical vertices using the interpolation method described in Takeuchi et al. (2009) (see Appendix D). Note that vertices more than 2 cm away from all of the cortical projection points had no NIRS data.

EEG experiments and preprocessing

Subjects were seated in a comfortable reclining armchair and performed brisk, self-initiated movements (extension and flexion) of the right index finger (more than about 3-s inter-movement interval). They completed six sessions, each consisting of 20 movements, resulting in a total of 120 movements. Subjects took brief (about 1 min) rests between sessions.

EEG was recorded at a sampling rate of 1024 Hz with a 64-electrode cap, referenced to the Common Mode Sense (CMS) active electrode. A Biosemi Active Two system was used for amplification and analog-to-digital conversion of the EEG signals. Electrooculography (EOG) data were also collected to control for eye movements.

Movement onset[3] was detected using an optical sensor (GP2Y0A21YK; SHARP, Japan); the subject's finger blocked the light in the resting state and unblocked it when he or she lifted the finger. The electrical output of the optical sensor unit was sent to the EEG system for signal averaging. Data from a later additional experiment revealed that movement onset detected by the optical sensor was delayed by 134 ± 23 ms relative to that detected by EMG in subject TA.

EEG sensor positions were measured before the EEG experiment using the stylus marker to allow subsequent co-registration of EEG, fMRI and NIRS results.

EEG signals were first passed through a band-pass filter (0.2–100 Hz) and a notch filter (50 Hz), and down-sampled to 250 Hz. Note that BP was eliminated using a high-pass filter of 0.2 Hz, because it reflects the early preparation stage and was therefore beyond the scope of this study. EEG signals between 1500 ms before and 200 ms after movement onset detected by the optical sensor were then extracted and baseline-corrected using the first 500 ms as a baseline. Finally, outlier trials and sensors were excluded from the analysis according to the following steps: (1) determining a threshold so that 95% of all absolute EEG signals are below the threshold, (2) excluding trials where absolute EEG signals

[3] In the present paper, 'movement onset' refers to movement onset detected by the optical sensor signal; 'EMG onset' refers to movement onset detected by EMG.

for >25% of sensors exceeded the threshold, (3) excluding sensors where absolute EEG signals for >25% of trials exceeded the threshold, (4) excluding trials where absolute EEG signals for at least one sensor were >120 μV. Consequently, the number of available trials was reduced from 120 to approximately 80 trials for each subject. The number of available sensors was 64 for subject TA and 62 for subject RO.

EEG signals after the above preprocessing were used for both the calculation of event-related potentials (ERPs) and for source current estimation with VBMEG.

Settings for VBMEG

As shown in the result section below, the hyper-parameter values $m_0 = 100$ and $\gamma_0 = 10$ performed relatively well in most situations. Therefore, we used these values for all cortical dipoles. In addition to the cortical dipoles, artifact dipoles located at the center of the left and right eyeballs were assumed in the estimation with VBMEG. The results of previous studies (Fujiwara et al., 2009; Morishige et al., 2009) suggested that the incorporation of artifact dipoles allowed the effective removal of eye-movement artifacts from EEG data. Hyper-parameter values of the prior estimate of the current variance of 10^2 [nAm]^2 and $\gamma_0 = 10^{4.5}$ were used for artifact dipoles, based on a previous study (Morishige et al., 2009).

The EEG time series from 1000 ms before to 200 ms after the movement initiation was analyzed to study the brain activity involved in the late preparation, execution and somatosensory information-processing stages of finger lifting (movement duration was about 500 ms). The time series data from 1500 ms to 1000 ms before the movement initiation were used to estimate the baseline of the current variance. Because the pattern of cortical activity was assumed to change according to the phase of movement (e.g., preparation, execution), the EEG time series was divided into 100-ms time-windows with 50-ms overlaps. Source current estimation with VBMEG was conducted for each series of divided EEG data under the assumption that the current variance was temporally invariant within each time window. Thus, the current variance changed every 50 ms, but the current was estimated every 4 ms (because the sampling rate was 250 Hz).

As described above, estimations with VBMEG were conducted for the combinations of three numbers of EEG sensors[4] (64-ch, 31-ch, 19-ch; Fig. 1) and three prior information types (fMRI prior, NIRS prior, no prior).

Evaluation of the performance of source current estimation with VBMEG

Because it is impossible to determine the true source current in real situations, the estimation accuracy measures that require true source positions and/or current amplitudes, such as the localization error, were not available for the real experimental data. We therefore evaluated the performance of VBMEG as follows. First, the estimated current for the combination of 64-ch EEG and fMRI was used as a reference, because previous studies demonstrated that VBMEG with fMRI prior yielded physiologically acceptable results in the case of MEG (Toda et al., 2011; Yoshioka et al., 2008). Then, variants of three metrics used in the simulation study were calculated by regarding the reference currents as substitutes of true currents. The first metric was the correlation coefficient (R_{st}) between the spatio-temporal pattern of the estimated current under the reference condition (i.e., the combination of 64-ch EEG and fMRI) and that under the comparison condition. The second metric was the correlation coefficient (R_s) between the temporally-averaged (during the 200 ms period just before movement onset) spatial pattern of the estimated current under the reference condition and that under the comparison condition. The third metric was the RMSE between the estimated current under the reference condition and that under the comparison condition. RMSE was calculated over the analysis time-windows (from 1000 ms before to 200 ms after onset).

[4] EEG data were obtained with a 64-electrode cap for both the 31-ch and 19-ch cases with no additional experiments.

Results

Results of computer simulations

First, we describe the results of the first step simulation, in which we investigated the effects of the types of prior information (no, missing, correct, and false positive priors) and the values of the hyper-parameters (m_0, γ_0), and their interactions. Then, we describe the results of the second step simulation, where we investigated the effects of the number of EEG sensors (64ch, 31ch, 19ch) and the resolution of the prior information ($R = 6$, 12, 18), and their interactions.

Results of the first step

Fig. 3 shows the results of ROC analysis. For the first source, S_1, two-way ANOVA revealed significant effects of the types of prior information [$F(3, 17{,}999) = 4184.99$, $p<0.05$] and the combinations of hyper-parameters [$F(8, 17{,}999) = 29.84$, $p<0.05$], and a significant interaction between these factors [$F(24, 17{,}999) = 42.99$, $p<0.05$]. For the second source, S_2, two-way ANOVA revealed significant effects of the types of prior information [$F(3, 17{,}999) = 3090.02$, $p<0.05$] and the combinations of hyper-parameters [$F(8, 17{,}999) = 13.03$, $p<0.05$], and a significant interaction between these factors [$F(24, 17{,}999) = 26.28$, $p<0.05$]. When the correct or false positive prior

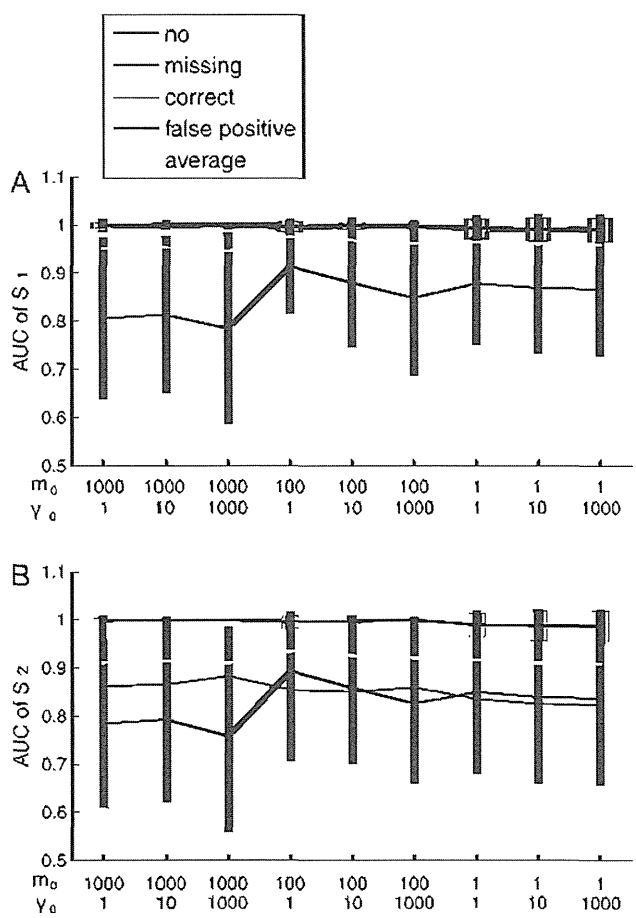

Fig. 3. Results of ROC analysis for the first step simulation. The Areas Under Curves (AUCs) for S_1 (A) and S_2 (B) are plotted against the combinations of hyper-parameters, for no prior (black line), missing prior (red line), correct prior (green line), and false positive prior (blue line). The yellow line is the average of all prior types. Error bars indicate SDs.

was used, the AUC was almost 1 (i.e., perfect detection) for both S_1 (Fig. 3A, green or blue line) and S_2 (Fig. 3B, green or blue line), regardless of the values of hyper-parameters tested in the present study (multiple comparison, $p>0.05$). When the missing prior was used, the AUC was almost 1 for S_1, which had correct active prior information, regardless of the values of hyper-parameters (multiple comparison, $p>0.05$; Fig. 3A, red line). However, the AUC for S_2, which had false inactive prior information, decreased to about 0.85 and changed with the values of hyper-parameters; roughly speaking, $m_0=1$, which is far smaller than the theoretical value of 674 in the present setting, yielded slightly lower AUC values (multiple comparison, $p<0.05$; Fig. 3B, red line). With no prior information, the AUC values for both S_1 and S_2 were both around 0.85 and changed with the values of hyper-parameters; roughly speaking, $m_0=1000$ yielded lower AUC values (multiple comparison, $p<0.05$; Figs. 3A and B, black lines). Taken together, these results indicate that an overly large or small value of m_0 (i.e., $m_0=1$ or 1000) can yield incorrect estimates, depending on the type of prior information.

Fig. 4 shows correlation coefficients (R_{st} and R_s) between true and estimated currents against the combination of hyper-parameters.

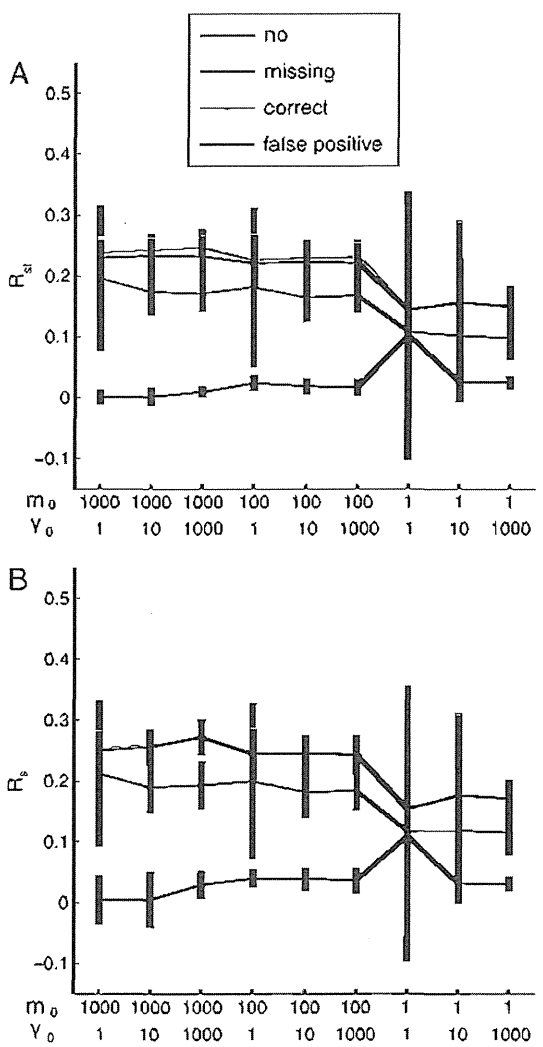

Fig. 4. Results of correlation analysis for the first step simulation. (A) Correlation coefficients between true and estimated spatio-temporal current patterns, R_{st}, are plotted against the combinations of hyper-parameters. (B) Correlation coefficients between true and estimated spatial current patterns, R_s, are plotted against the combinations of hyper-parameters. The line colors are the same as those in Fig. 3. Error bars indicate SDs.

Both R_{st} and R_s showed similar tendencies. For R_{st}, a two-way ANOVA showed significant effects of the types of prior information [$F(3, 17{,}999)=4797.31$, $p<0.05$] and the combinations of hyper-parameters [$F(8, 17{,}999)=186.74$, $p<0.05$] and a significant interaction between these factors [$F(24, 17{,}999)=79.22$, $p<0.05$]. For R_s, there were significant effects of the types of prior information [$F(3, 17{,}999)=4971.55$, $p<0.05$] and the combinations of hyper-parameters [$F(8, 17{,}999)=209.96$, $p<0.05$] and a significant interaction between these factors [$F(24, 17{,}999)=77.64$, $p<0.05$]. Both correlations were far higher when the prior was available compared to when it was unavailable, even if the prior included wrong information. When the prior was available, both correlations were lower with $m_0=1$, the value furthest away from the theoretical value of 674, and the SDs of both correlations were larger with $\gamma_0=1$.

Fig. 5 shows the RMSE against the combination of hyper-parameters. Two-way ANOVA revealed significant effects of the types of prior information [$F(3, 17{,}999)=2.8696\times10^6$, $p<0.05$] and the combinations of hyper-parameters [$F(8, 17{,}999)=1.1897\times10^6$, $p<0.05$], and a significant interaction between these factors [$F(24, 17{,}999)=1.2042\times10^6$, $p<0.05$]. When the prior was not available, errors were markedly large with $m_0=1000$ regardless of the value of γ_0 (Fig. 5).

The effect of the types of prior information can be summarized as follows. The performance of VBMEG was markedly better when the prior information was available compared to when it was unavailable, even if it contained incorrect information. Estimation with VBMEG was relatively robust for the false positive prior but vulnerable to the missing prior, especially for the source with false inactive prior (i.e., S_2).

It is difficult to determine the best combination of hyper-parameters because the estimation performance was not severely affected by the combination of hyper-parameters when prior information was available. Regarding the magnification parameter, m_0, we observed the following tendency. Overly small values of m_0 (i.e., $m_0=1$) sometimes yielded incorrect estimates, even when the correct prior was available (e.g., see Fig. 4). The largest value of m_0 (i.e, $m_0=1000$) yielded good estimates when the prior was available, but yielded

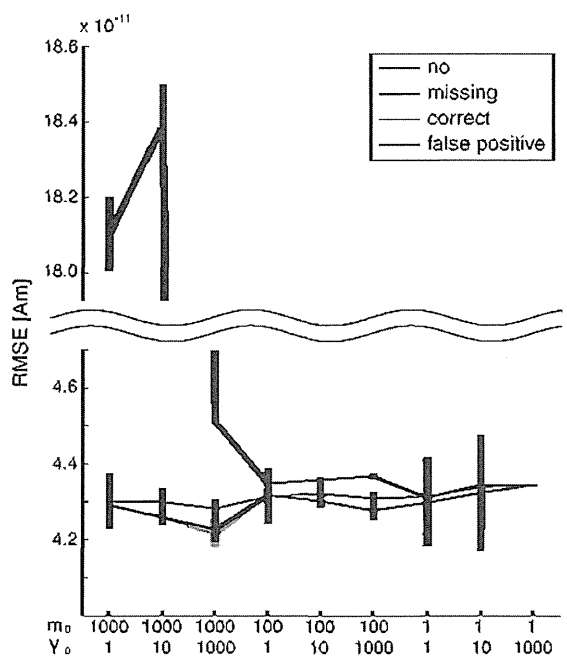

Fig. 5. The root mean squared errors (RMSE) between true and estimated spatio-temporal current patterns are plotted against the combinations of hyper-parameters, for all types of priors. The line colors are the same as those in Fig. 3. Error bars indicate SDs.

incorrect estimates when the prior was not available (see Fig. 5). These findings suggest that a moderate value of m_0 (i.e., $m_0 = 100$) should be adopted. Regarding the confidence parameter, γ_0, the smallest value of γ_0 (i.e., $\gamma_0 = 1$) sometimes yielded unstable estimates (i.e., SDs of evaluation metrics were large; e.g., see Fig. 4). Because the spatial resolution and localization accuracy of NIRS are limited by measurement geometry to 3 cm, a lower value of γ_0 should be used in the experimental data analysis. Therefore, we chose to use $[m_0, \gamma_0] = [100, 10]$ instead of $[m_0, \gamma_0] = [100, 1000]$ in both the second step simulation and experimental data analysis. An additional reason for adopting $[m_0, \gamma_0] = [100, 10]$ is that this combination has yielded valid results in previous studies (Fujiwara et al., 2009; Toda et al., 2011).

Results of the second step

Fig. 6 shows the results of ROC analysis for S_1 (Fig. 6A) and S_2 (Fig. 6B). The AUC value was very close to 1 (perfect detection), regardless of the resolution of prior information or the number of EEG sensors. For S_1, two-way ANOVA revealed a significant effect of the resolution of prior information [$F(2, 4499) = 200.69$, $p < 0.05$], but revealed no significant effect of the number of EEG sensors [$F(2, 4499) = 0.68$, $p = 0.5068$] or a significant interaction between these factors [$F(4, 4499) = 1$, $p = 0.4074$]. Also for S_2, two-way ANOVA revealed a significant effect of the resolution of prior information [$F(2, 4499) = 109.26$, $p < 0.05$], but did not reveal a significant effect of the number of EEG sensors [$F(2, 4499) = 0.45$, $p = 0.6393$] or a significant interaction between these factors [$F(4, 4499) = 1.54$, $p = 0.1872$]. These results suggest that, when the correct prior was available, detection improved with the resolution of prior information, whereas it hardly changed with the number of EEG sensors.

Fig. 7A shows the results for R_{st}. Two-way ANOVA revealed significant effects of the resolution of prior information [$F(2, 4499) = 25{,}122.9$, $p < 0.05$] and the number of EEG sensors [$F(2, 4499) = 117.68$, $p < 0.05$], but interaction between these factors was not significant [$F(4, 4499) = 1.32$, $p = 0.2617$]. The correlation became lower as the spatial resolution of the prior worsened and as the number of EEG sensor decreased (multiple comparison, $p < 0.05$). The lowest correlation,

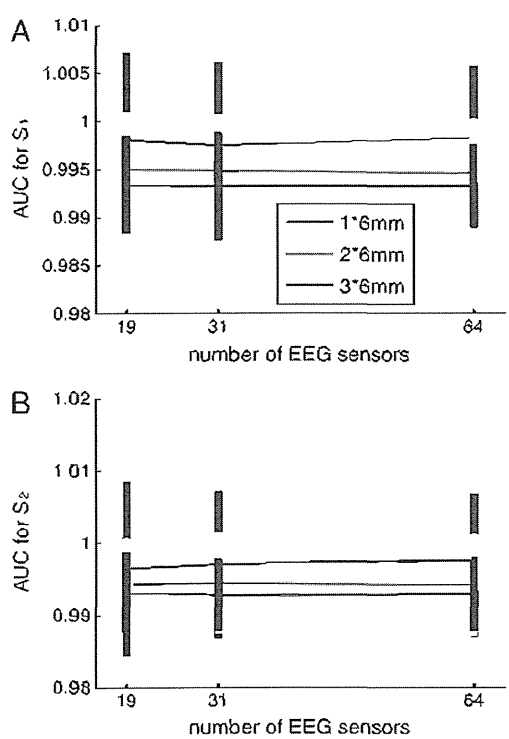

Fig. 6. Results of ROC analysis for the second step simulation. The AUCs for S_1 (A) and S_2 (B) are plotted against the number of EEG sensors, for R = 6 (red), R = 12 (green), and R = 18 (blue). Error bars indicate SDs.

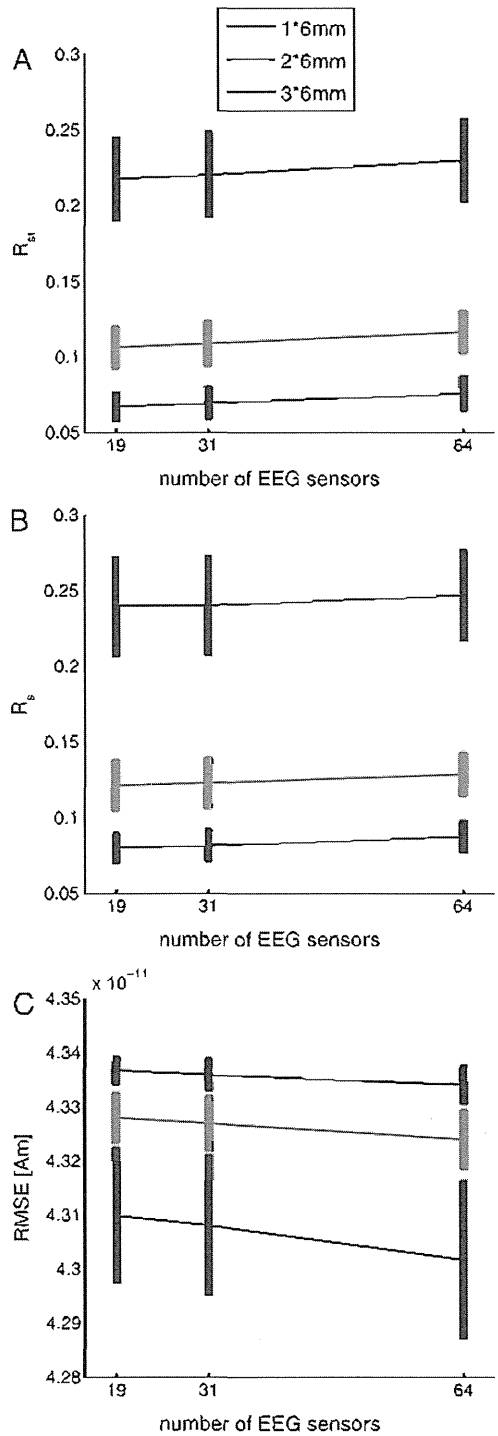

Fig. 7. Results of correlation analysis and RMSE analysis for the second step simulation. The evaluation metrics are plotted against the number of EEG sensors. The line colors are the same as those in Fig. 6. (A) The correlation coefficients of spatio-temporal patterns, R_{st}. (B) The correlation coefficients of spatial patterns, R_s. (C) The root mean squared errors, RMSE. Error bars indicate SDs.